Energy Storage

WILEY

ENERGY STORAGE

RESEARCH ARTICLE

Hydrogen Storage Performance of Sunflower Stalk-Derived Activated Carbons Produced via $ZnCl_2$ and KOH Activation

Pınar Turan Beyli[1] | Mehmet Doğan[1] | Zeynep Bicil[1] | Yasemin Turhan[1] | Ersin Yanmaz[2] | Berna Koçer Kizilduman[1]

[1]Faculty of Science and Literature, Department of Chemistry, Balikesir University, Balikesir, Turkey | [2]Altınoluk Vocational School, Department of Chemical and Chemical Processing Technologies, Balikesir University, Balikesir, Turkey

Correspondence: Mehmet Doğan (mdogan@balikesir.edu.tr; mdogan7979@gmail.com)

Received: 2 July 2025 | **Revised:** 13 August 2025 | **Accepted:** 25 August 2025

Funding: This work was supported by Balikesir University (Project Number: BAP2018/105).

Keywords: characterization | hydrogen storage | isotherm | kinetics | optimization | sunflower stalk

ABSTRACT

In this study, the hydrogen storage capacities of activated carbons derived from sunflower stalk wastes were enhanced by initial chemical activation using different activating agents ($ZnCl_2$ or KOH) at biomass ratios of 1:1, 2:1, and 3:1 (w/w), followed by carbonization at varying temperatures (600°C, 700°C, 800°C, and 900°C) based on their surface area performance. The optimization and characterization of the prepared samples were systematically conducted using BET, FTIR, DTA/TG, and SEM/EDX techniques. SEM/EDX analysis revealed a marked increase in porosity and notable alterations in the elemental composition of the activated carbon surfaces as a function of the activating agent and carbonization temperature. Hydrogen storage capacities of the optimized samples were measured as a function of pressure at both room and cryogenic temperatures. As a result of the optimization process, the samples with the highest surface areas were identified as AC-Z2-700 and AC-K2-700, with AC-Z2-700 exhibiting the highest hydrogen storage performance. Storage capacities increased with rising pressure and decreasing temperature for both samples, while the isotherm profiles varied significantly between room and cryogenic conditions. The experimental data fitted well with the Henry and Freundlich isotherms at room temperature and with the Langmuir isotherm at cryogenic temperature. Furthermore, kinetic analyses indicated that the adsorption followed a pseudo-second-order model and that the dominant mechanism was intraparticle diffusion within the pores of the activated carbon. Overall, the findings demonstrate that sunflower stalk is a promising and sustainable precursor for producing high-surface area activated carbons with competitive hydrogen storage capabilities, contributing to both clean energy applications and environmental sustainability.

1 | Introduction

Energy plays an essential role in fostering economic growth, social welfare, and environmental sustainability, serving as a cornerstone of modern society. It directly influences quality of life by underpinning nearly every sector. Present-day energy demand is met through a variety of sources, including fossil fuels (oil, natural gas, coal), renewable resources (solar, wind, hydro, biomass), and nuclear power. However, the heavy reliance on fossil fuels, their finite reserves, and the environmental issues associated with their use have heightened the urgency of developing clean and sustainable energy carriers [1]. Renewable energy sources offer inexhaustible and environmentally benign alternatives that can reduce greenhouse gas emissions while enabling long-term energy production. Nevertheless, their variable and intermittent supply profiles create challenges for continuous energy delivery, making efficient storage systems indispensable. One promising approach to overcoming this intermittency is to store renewable energy in the form of hydrogen, which can stabilize supply and enhance energy security. Hydrogen stands out among all known fuels due to its exceptionally high gravimetric energy density (33.59 kWh kg^{-1}) and its ability to produce only water upon utilization, making it an attractive carbon-neutral option for both stationary and mobile applications [2–4]. Current storage methods include high-pressure gas cylinders, cryogenic liquid storage, and chemical storage within compounds such as metal hydrides. However, each method has inherent limitations: high-pressure systems require robust containment and raise safety concerns, cryogenic storage demands extremely low temperatures with substantial energy penalties, and chemical storage often involves complex and energy-intensive hydrogen release processes [5, 6].

Given these constraints, solid-state adsorption using porous materials has gained increasing attention as an alternative [7]. Among the various adsorbents investigated, such as zeolites [8], metal–organic frameworks (MOFs) [9], and carbon-based nanostructures including graphene [10, 11], carbon nanotubes [6, 12–14], and fullerenes [15], activated carbon (AC) has emerged as a cost-effective and efficient hydrogen storage medium. This is largely due to its high specific surface area, tunable microporosity, low production cost, and the abundance of biomass feedstocks. Agricultural residues, including almond shells [16], olive stones [17], horse chestnut shells [18], pomegranate peels [19], lignin wastes [20], and tangerine peels [21], are particularly attractive as AC precursors because they are renewable, inexpensive, and their valorization mitigates the environmental issues associated with uncontrolled disposal [22].

Sunflower stalks, in particular, present a distinctive lignocellulosic composition with high cellulose, moderate lignin, and low hemicellulose content [23, 24]. This composition facilitates the development of large surface areas and microporous structures during chemical activation, while the inherently low ash content minimizes pore blockage. These structural attributes can improve hydrogen adsorption by increasing the number of accessible sites and enhancing gas diffusion pathways, making sunflower stalks a promising and underexplored precursor for high-performance ACs. Although AC production from sunflower stalks has been reported, no study has yet investigated their hydrogen storage performance, representing a significant knowledge gap. Previous works have demonstrated AC synthesis from sunflower stalks using hydrothermal carbonization, yielding surface areas up to 1505 $m^2 g^{-1}$ and total pore volumes of 0.94 $cm^3 g^{-1}$ [25], and from sunflower pith via NaOH and KOH activation, achieving BET surface areas of 2690 $m^2 \cdot g^{-1}$ and 2090 $m^2 \cdot g^{-1}$, respectively [26]. Microwave-assisted K_2CO_3 activation of sunflower seeds produced AC with 1411.55 $m^2 g^{-1}$ surface area [27]. Studies on other biomass sources have shown that activation conditions strongly influence hydrogen uptake: almond shell-derived AC (AC600) reached 2.53 wt% at 77 K and 27 bar via microwave-assisted chemical activation [16], while $ZnCl_2$-activated horse chestnut shell AC achieved 4.46 wt% at 77 K with a surface area of 2270 $m^2 g^{-1}$ [18]. Similarly, $ZnCl_2$-activated tangerine peel-derived carbons displayed enhanced low-temperature hydrogen storage capacities due to higher surface areas compared to KOH-activated counterparts [21]. Although $ZnCl_2$ activation generally yields higher surface areas and improved hydrogen adsorption at cryogenic temperatures, its interaction with sunflower stalks owing to their distinctive cellulose/lignin/ash profile may produce unique pore architectures. The present work systematically compares $ZnCl_2$ and KOH activation of sunflower stalks under identical conditions, correlating BET surface area, pore structure, surface chemistry, and hydrogen storage performance. Based on these considerations, the objectives of this study were to: (i) synthesize ACs from sunflower stalk biomass using $ZnCl_2$ and KOH chemical activation and compare their surface characteristics, (ii) elucidate the effects of different activation mechanisms ($ZnCl_2$-induced dehydration vs. KOH-induced etching) on pore development, surface chemistry, and C/O ratio, (iii) characterize the obtained ACs using BET surface area analysis, pore size distribution, FTIR, DTA/TG, and SEM/EDX, (iv) evaluate hydrogen storage capacities under various pressures and temperatures, comparing results with literature data for other biomass-derived ACs, and (v) investigate adsorption kinetics and diffusion mechanisms using model equations (pseudo-first order, pseudo-second order, Weber–Morris, Boyd) to relate them to storage performance. This integrated approach, combining detailed physicochemical characterization with adsorption kinetics, aims not only to quantify storage capacity but also to clarify the underlying hydrogen adsorption mechanism in sunflower stalk-derived ACs.

2 | Material and Methods

2.1 | Materials

Sunflower stalks were obtained from agricultural lands within the borders of Balıkesir province. All chemicals to be used in the study were purchased in analytical purity and used without further purification.

2.2 | Methods

2.2.1 | Activated Carbon Production

Sunflower stalks were first dried in a 70°C oven for 2 days. The dried samples were ground in a Retsch PM100 model ball mill at 500 rpm for 30 min and sieved through a 100 μm sieve in a Retsch AS200 sieving device. Sunflower stalks with grain sizes of 0–100 μm were used in the production of AC. The dried, ground, and sieved sunflower stalks with grain sizes of < 100 μm were soaked with 50 mL of water in a mixture of chemical activation agents (KOH and $ZnCl_2$) at a ratio of 1/1, 2/1, and 3/1 by mass (chemical activation agent/sunflower stalk) and kept at room temperature for 1 day. Then, the sunflower stalks soaked with the activation agent were dried in an oven at 110°C for 1 day. The dried samples were pyrolyzed at a heating rate of 5°C min^{-1} for 2 h under 10 psi constant N_2 flow in a stainless steel reactor vessel at 700°C for agent/sunflower stalk optimization, and then the samples were allowed to cool under 10 psi constant N_2 flow. The cooled samples were initially treated with a 0.1 M hydrochloric acid solution, followed by successive washings with hot and distilled water until the filtrate reached a neutral pH range of 6–7. After washing, the samples were dried in an oven at 110°C for 24 h. BET surface areas of the dried samples were measured. The same procedures were carried out at 600°C, 700°C, 800°C, and 900°C for the sample with the highest surface area to optimize the pyrolysis temperature. BET surface areas of the pyrolyzed samples were measured again. In this way, the hydrogen storage capacities of the highest surface area samples optimized according to BET surface areas were measured [17, 19, 28].

2.2.2 | Hydrogen Storage

Hydrogen adsorption–desorption measurements were carried out using a Hiden IMI-PSI gas adsorption system (Hiden Isochema Ltd., UK). Prior to measurements, the samples were degassed under vacuum at 250°C for 4 h. Experiments were performed at 77 K (liquid nitrogen) and 298 K in the pressure range of 0–100 bar. The instrument has a pressure accuracy of ±0.1% of full scale and a temperature stability of ±0.1°C. To ensure repeatability, each storage measurement was conducted in triplicate under identical experimental conditions, and the average values are reported. The standard deviation of the measured storage capacities was within ±2.5% of the mean value, confirming the high reliability and consistency of the measurements [29, 30].

2.3 | Characterization

2.3.1 | BET Surface Area

Before BET surface area measurements and pore size analyses of the samples were performed, the samples were degassed at 250°C for 24 h. Surface area measurements and pore size distributions of the degassed samples were performed using a Quantachrome Nova 2200e series device using pure nitrogen gas as an adsorbate in a liquid nitrogen environment (77 K).

2.3.2 | FTIR-ATR Analysis

FTIR-ATR spectra of the samples were taken in the wavelength range of 650–4000 cm^{-1} using the PerkinElmer Spektrum 100 device.

2.3.3 | DTA/TG Analysis

Thermal properties of sunflower stalks and the optimized ACs were carried out using PerkinElmer Diamond DTA/TG instrument in the range of 25°C–1200°C under nitrogen atmosphere.

2.3.4 | SEM/EDX Images

The surface morphology of ACs derived from sunflower stalks was imaged using a Zeiss EVO LS 10 Scanning Electron Microscope operating at an accelerating voltage of 20 kV with various magnification levels. Prior to imaging, powder samples were placed onto an SEM holder using double-sided electrically conducting carbon adhesive tape and rendered conductive through the application of an Au/Pd coating via a sputter coater at 20 mV for a duration of 60 s. Furthermore, the elemental compositions of the samples were assessed employing a Bruker EDX detector. Figure 1 shows the flow diagram of the study.

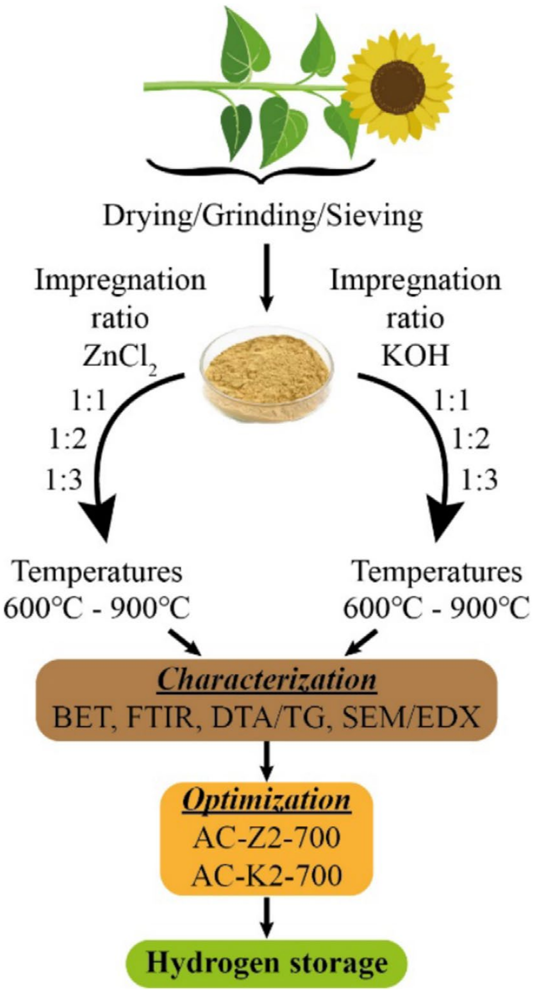

FIGURE 1 | Flow diagram of the study.

3 | Results and Discussion

3.1 | Characterization

Activated carbons produced from sunflower stalks with different chemical agents at different carbonization temperatures were tried to optimize with BET, FTIR, DTA/TG, and SEM/EDX devices.

3.1.1 | BET Analysis

Figure 2 shows the N$_2$ adsorption/desorption isotherms of ACs produced from sunflower stems at different agent ratios and activation temperatures with ZnCl2 and KOH activations. BET surface areas and pore volumes of ACs produced from sunflower stalks by chemical and carbonization activation methods are given in Table 1. The N$_2$ adsorption/desorption isotherms of the AC samples exhibit a combination of Type I and Type IV features, as defined by the IUPAC classification [31]. The pronounced uptake observed at low relative pressures ($P/P_0 < 0.1$) indicates a high proportion of micropores, while

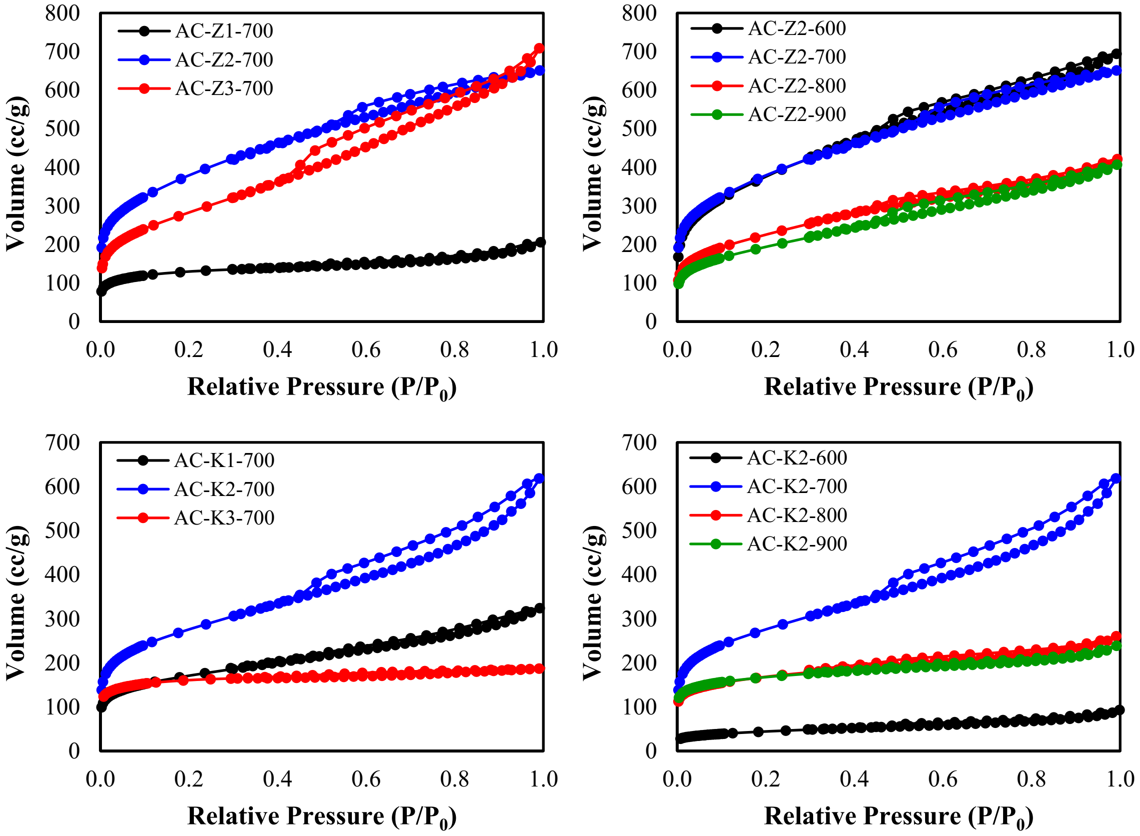

FIGURE 2 | N_2 adsorption/desorption isotherms of activated carbons produced from sunflower stems with $ZnCl_2$ and KOH activations at different agent ratios and activation temperatures.

TABLE 1 | BET surface areas and pore volumes of activated carbons produced under different conditions.

Samples	Agents	Agents: sunflower stalk ratios	Temperatures	S_{BET} (m^2/g)	V_t (cc/g)	V_{DFT} (cc/g)	V_{micro} (cc/g)	V_{mezo} (cc/g)
AC-Z1-700	$ZnCl_2$	1:1	700	475	0.32	0.29	0.24	0.05
AC-Z2-700	$ZnCl_2$	2:1	700	1368	1.01	0.93	0.71	0.22
AC-Z3-700	$ZnCl_2$	3:1	700	1016	1.01	0.99	0.54	0.45
AC-Z2-600	$ZnCl_2$	2:1	600	1352	1.08	0.98	0.73	0.25
AC-Z2-800	$ZnCl_2$	2:1	800	807	0.65	0.59	0.43	0.16
AC-Z2-900	$ZnCl_2$	2:1	900	693	0.63	0.57	0.36	0.21
AC-K1-700	KOH	1:1	700	618	0.50	0.46	0.32	0.14
AC-K2-700	KOH	2:1	700	986	0.96	0.88	0.53	0.35
AC-K3-700	KOH	3:1	700	608	0.29	0.26	0.25	0.01
AC-K2-600	KOH	2:1	600	157	0.14	0.12	0.08	0.04
AC-K2-800	KOH	2:1	800	613	0.40	0.35	0.30	0.05
AC-K2-900	KOH	2:1	900	620	0.37	0.32	0.29	0.03

the well-defined hysteresis loop appearing in the intermediate-to-high relative pressure region ($P/P_0 \approx 0.4–0.9$) reflects the contribution of mesopores and the occurrence of capillary condensation. Optimization of the synthesis parameters yielded AC-Z2-700 and AC-K2-700 as the most promising samples, outperforming other variants in adsorption capacity, micropore volume, and balanced micro/mesopore ratio. AC-Z2-700, benefitting from $ZnCl_2$ activation, developed a more advanced microporous network, resulting in superior adsorption performance at low relative pressures. In contrast, AC-K2-700,

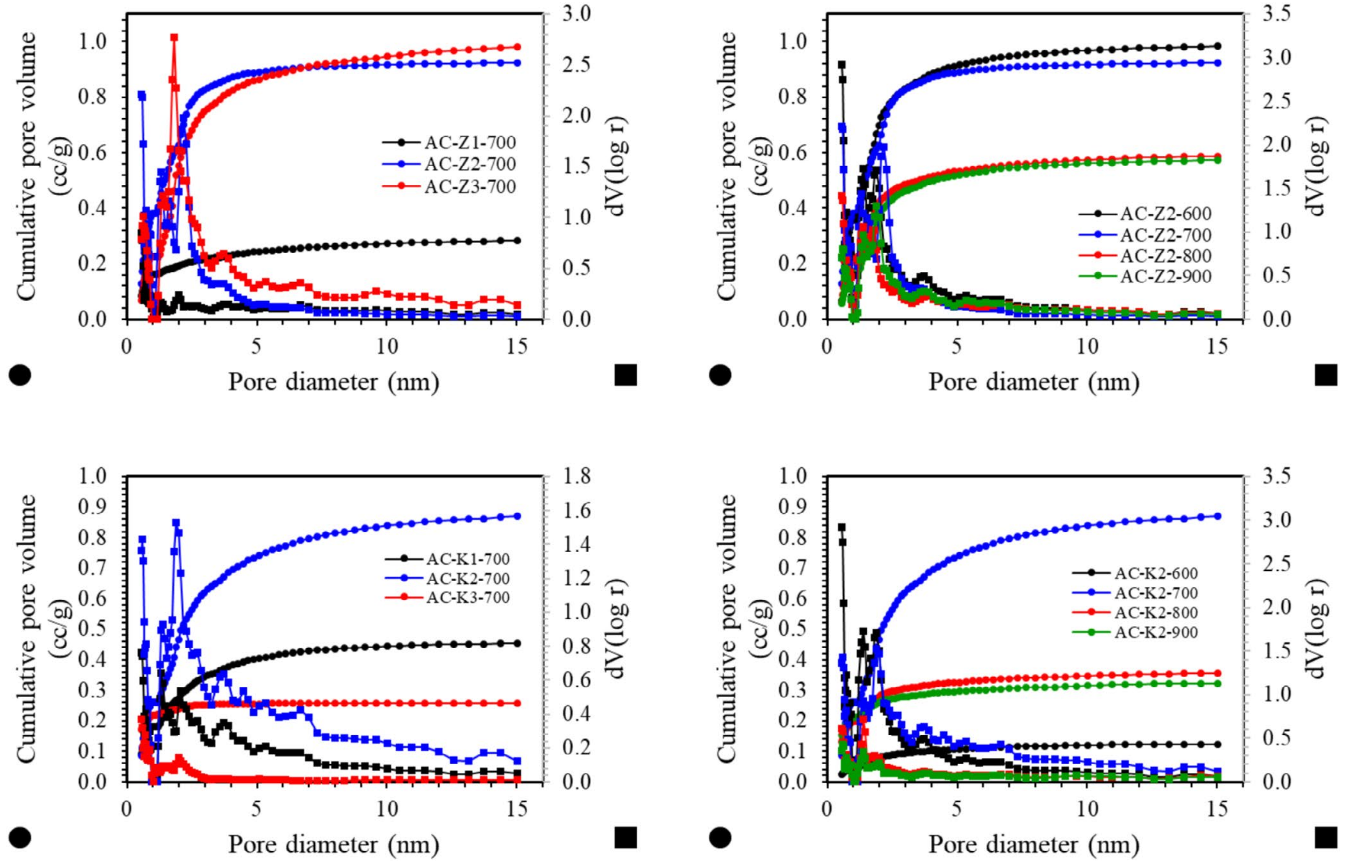

FIGURE 3 | The changing of cumulative pore volumes of activated carbon samples versus pore diameter.

produced via KOH activation, displayed a distinct hysteresis behavior linked to its unique pore morphology. Collectively, these results demonstrate that both optimized samples possess high surface areas, well-distributed pore structures, and favorable adsorption kinetics, making them strong candidates for hydrogen storage applications. Figure 3 shows the changes in cumulative pore volume of the produced ACs against pore diameter. KOH and $ZnCl_2$ were used as chemical agents in the production of AC. 600°C, 700°C, 800°C, and 900°C were selected as carbonization temperatures. In the production of AC, the samples were first activated at 1:1, 2:1, and 3:1 chemical agents by mass (KOH or $ZnCl_2$)/sunflower stalk ratios and subjected to carbonization at 700°C. BET surface areas of the produced samples were measured and pore volumes were calculated according to the DFT method. The results showed that among the ACs produced by both KOH and $ZnCl_2$ activation, the sample with the highest BET surface area was the sample produced at 700°C at a ratio of 2:1. BET surface areas of AC-K2-700 and AC-Z2-700 were determined as 986 and 1368 m^2/g, respectively. Again, when Table 1 is examined, it is seen that both samples consist of micro and mesopores. While the micro and mesopore volumes of AC-K2-700 are 0.53 and 0.35 cc/g, those of AC-Z2-700 are 0.71 and 0.22 cc/g. When BET surface areas for both samples are compared, AC-Z2-700 has a higher BET surface area. KOH significantly affects biomass in AC production by affecting pore development and surface properties [32]. Activation with KOH promotes the development of both microporous and mesoporous structures. As the concentration of KOH increases, the specific surface area and pore volume of the obtained AC also increase. From Table 1, it is seen that when the KOH/biomass ratio increases, both the surface area and pore volume increase. KOH increases the porosity of the carbon by creating active points on the surface of the carbon. In this process, KOH breaks some bonds in the structure of the carbon, causing more pores to open and the surface area to increase. However, it is also stated that too much increase in the KOH ratio leads to deterioration of the pore structure [33]. $ZnCl_2$ is an effective chemical activating agent used to produce AC from various plant-based materials [17–19]. It is observed that the impregnation ratio of $ZnCl_2$ to biomass and the carbonization temperature significantly affect the surface area of the produced AC. There may be several reasons why $ZnCl_2$ creates a more porous and high surface area structure. During the impregnation stage, $ZnCl_2$ promotes the dehydration of cellulosic material. During carbonization, this dehydration leads to the charring and aromatization of carbon structures, resulting in the formation of porous structures [34]. $ZnCl_2$ prevents tar formation and promotes aromatization, resulting in porous AC [35]. $ZnCl_2$ increases the carbon content of AC. High carbon content provides more voids and surface area, which promotes pore formation [36]. $ZnCl_2$ promotes the transformation from mesopores to micropores, which leads to the change of the surface structure of AC and the formation of narrower slit-like pores [37]. After optimization of the activation agent ratio, the obtained sample was subjected to heat treatment under an inert atmosphere at different carbonization temperatures. It was determined that the samples with the highest BET surface area among the produced ACs were AC-Z2-700 and AC-K2-700. The activation agent ratio of 2:1 combined with an activation temperature of 700°C provides an optimal balance between activation intensity and structural integrity. At this ratio, sufficient reaction between the activating agent and the carbon precursor occurs, leading to the development of a well-defined micro- and mesoporous network and achieving the maximum BET surface area. Lower ratios result in insufficient activation, limiting pore formation and surface area. Conversely, higher ratios or activation temperatures above 700°C can cause excessive etching of the carbon framework, leading to pore widening, merging, or even collapse, thereby reducing the overall surface area. The temperature of 700°C provides enough thermal energy for uniform pore formation while preventing severe structural degradation, ensuring the highest accessible surface area for hydrogen adsorption. It is seen in the literature that the optimal conditions vary depending on the raw material, but in general, ACs with higher BET surface areas are produced at higher impregnation ratios and medium temperatures. For example, while AC with 946 m^2/g surface area was produced from peach pit at 500°C at a ratio of 3:1 [38], AC with 2170 m^2/g surface area was produced from sheep manure at 400°C at a ratio of 3:1 [39]. $ZnCl_2$ activation tends to preserve the aromatic structure of carbon better than KOH activation, resulting in the formation of structures with higher micropore volumes [40]. These findings indicate that $ZnCl_2$ is an effective activating agent for producing high-quality AC from various biomass sources. Samples optimized with respect to BET surface areas and pore volumes were used in hydrogen storage analyses. Similarly, Ateş and Özcan found that $ZnCl_2$ activation of poplar sawdust produced higher surface areas (1100 m^2/g) than KOH activation (761 m^2/g) [41]. Suhdi and Wang observed that $ZnCl_2$ activation of rubber fruit peels produced higher specific surface areas than KOH activation at all impregnation ratios [42].

3.1.2 | FTIR Analysis

FTIR spectra of ACs prepared under varying chemical agent ratios and activation temperatures reveal significant structural transformations compared to the sunflower stalk. The disappearance of characteristic cellulose and lignin absorption bands, along with the emergence of new peaks, indicates the decomposition of the plant's original biopolymeric structure and the formation of new functional groups characteristic of AC. FTIR spectra of ACs produced from sunflower stalk with different chemical agents under different conditions are presented in Figure 4. FTIR spectrum of the sunflower stalk exhibits characteristic absorption bands associated with its main biopolymeric components, including cellulose, hemicellulose, and lignin. A broad absorption band around 3337 cm^{-1} is attributed to O—H stretching vibrations from hydroxyl groups, while the peak near 2904 cm^{-1} corresponds to C—H stretching vibrations of aliphatic structures, with additional bending vibrations appearing at 1452, 1425, and 1314 cm^{-1}. The peak observed at 1682 cm^{-1} is assigned to C═O stretching vibrations, indicating the presence of carbonyl-containing functional groups such as ketones, aldehydes, and carboxylic acids. The peaks at 1609 and 1512 cm^{-1} correspond to aromatic C═C stretching, which are characteristic of lignin. Additionally, strong and broad peaks at 1056 and 1030 cm^{-1} are attributed to C—O stretching vibrations, primarily originating from cellulose and hemicellulose. The peak at 897 cm^{-1} has been associated with twisting vibrations between aromatic carbon and hydroxyl groups, while the peak at 661 cm^{-1} is linked to O—H twisting vibrations [43].

FTIR spectra of ACs synthesized using KOH as an activating agent show the disappearance of the O—H stretching (~3337 cm^{-1}), aliphatic C—H stretching (~2904 cm^{-1}), and C—O stretching (~1030 cm^{-1}) vibrations, suggesting the degradation of cellulose and lignin during activation. Instead, a distinct peak emerges in the 1530–1560 cm^{-1} range, corresponding to C═C stretching vibrations, which are characteristic of graphitic and aromatic structures, indicating the formation of an extended conjugated π-electron system. When analyzing FTIR spectra of ACs produced at different temperatures, a similar C═C stretching vibration around 1530 cm^{-1} is observed, reinforcing the presence of conjugated aromatic structures at moderate activation temperatures. However, as the activation temperature increases, this peak gradually diminishes and eventually disappears. This shift suggests that at elevated temperatures, C═C bonds undergo structural degradation, leading to the formation of aliphatic functionalities. The loss of aromatic C═C vibrations at high temperatures implies increased carbonization and possible graphitization, resulting in a material with a different surface chemistry and functional group distribution [44].

A similar trend is observed in ACs produced using $ZnCl_2$ as an activating agent. FTIR spectra confirm that lignin and cellulose-derived peaks disappear, while C═C stretching vibrations appear in the 1530–1560 cm^{-1} range, indicating the formation of aromatic structures. Additionally, C—O stretching vibrations are detected in the 1070–1100 cm^{-1} range, further supporting the development of oxygen-containing functional groups during activation. These results demonstrate that both the choice of activating agent and temperature significantly influence the structural and chemical composition of the resulting AC. Regardless of the activating agent used, the loss of cellulose and lignin characteristic peaks and the emergence of C—C and C—O vibrational bands confirm the successful conversion into a carbonaceous structure [16].

3.1.3 | DTA/TG Analysis

Thermal gravimetric analysis plays an important role in understanding biomass behavior and optimizing AC production by revealing mass loss events and chemical transformations during thermal processes. It also provides information on the pyrolysis of biomass in nitrogen or air atmosphere. Thermograms of the thermal gravimetric analysis of the sunflower stalk and the optimized samples were carried out in the range of 25°C–1200°C and given in Figure 5a,b. The data obtained from these thermograms are summarized in Table 2. The most general way to analyze the results obtained from non-isothermal thermogravimetric measurements of biomass and ACs is to show the mass loss-temperature (TG) curve. From this curve, the residue at the final temperature can be obtained quantitatively, and it is seen at what temperatures thermal decomposition occurs. The thermal characteristic behavior of a sample and the separation of different masses from this sample at various temperatures become more apparent in the mass loss-temperature (differential or d[TG]) curve. Since both curves are important for understanding

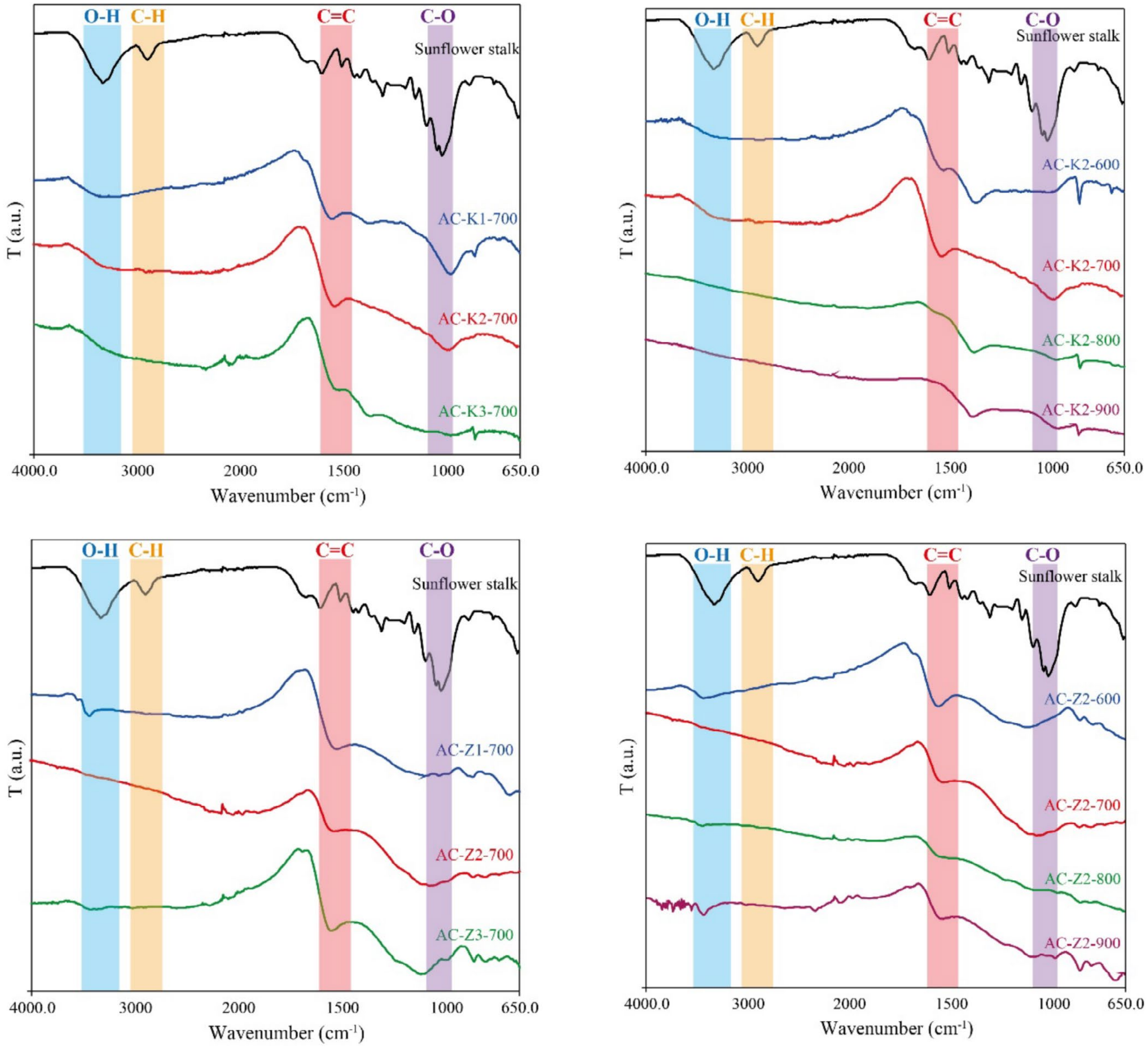

FIGURE 4 | FTIR spectra of activated carbons produced from sunflower stems with $ZnCl_2$ and KOH activations at different agent ratios and activation temperatures.

the thermal behavior, the data obtained from both curves are discussed. Lignocellulosic biomass typically contains cellulose, hemicellulose, and lignin. According to the literature, the mass losses observed in TG-d[TG] thermograms are related to the content of the biomass [45]. The first mass loss due to water loss from the sample is completed up to 200°C, and this step is the preheating stage. This temperature value varies from biomass to biomass. In this study, the sunflower stalk completed this stage up to 200°C, in accordance with the literature, and it is clear from Figure 5a that it showed a mass loss of approximately 6.7% [46]. In the second step, where the second mass loss occurs, lighter volatile substances are removed from the biomass structure between 200°C and 320°C. This step is defined as hemicellulose and cellulose decomposition [45, 46]. Hemicellulose pyrolysis is completed up to 350°C, while cellulose pyrolysis is completed between 250°C and 500°C [35]. Cellulose decomposes in a narrow temperature range and gives a sharp, single d[TG] peak, and this behavior is consistent with the simple chemical structure of cellulose. In Figure 5a, which shows the pyrolysis of sunflower stalk under nitrogen atmosphere, the second step is completed in the range of 180°C–600°C. The temperature at which the maximum mass loss occurs is 301.3°C, and the mass loss is approximately 62%. Lignin, which represents heavier volatile substances, is relatively more thermally stable than hemicellulose and cellulose, and is the most valuable component in the production of AC from biomass due to its carbon content, since it is converted to phenolic substances. Therefore, lignin pyrolysis occurs in a pyrolysis temperature range of 150°C–900°C, and no sharp mass loss peak is observed [35]. The maximum mass loss caused by lignin in the pyrolysis of sunflower stalk occurred at T_{max} value of 749°C, and the calculated mass loss was about 14%. The residue determined as a result of the analysis carried out in the range of 25°C–1200°C was about 16%. This is due to the carbonized carbon structure.

Activated carbons were produced from sunflower stalk using basic potassium hydroxide (KOH) and acidic zinc chloride ($ZnCl_2$) as activation agents. The physicochemical properties of AC also differ depending on the operating conditions and the agent used in chemical activation in AC production [47]. Thermograms showing TG and d[TG] curves of two optimized ACs are given in Figure 5b. From the general profile, it is seen that the degradation mechanism of the AC samples consists of four steps when $ZnCl_2$ agent is used and three steps when KOH is used. These maximum degradation temperatures were observed as 61.6°C, 255.6°C, 677.3°C, and 898.5°C for AC-Z2-700, respectively. The mass losses in four steps for this sample are 2.6%, 1.6%, 34.0%, and 14.5%, respectively. The residue at 1200°C was recorded as 50.9%. The maximum decomposition temperatures for AC-K2-700 are 62.6°C, 671.7°C, and 943.4°C. The maximum mass losses in three steps for the same sample are 5.8%, 22.4%, and 24.9%, respectively. The residue recorded at 1200°C is 46.7%. Studies show that the effectiveness of KOH and $ZnCl_2$ activation may vary depending on the biomass source [48–50]. In this study, better results in terms of surface area and porosity development were generally obtained for $ZnCl_2$. This tendency may have affected the thermal stability of ACs and caused them to decompose with a different mechanism. During the carbonization of $ZnCI_2$-impregnated biomass, $ZnCI_2$ works as a dehydrating agent. Dehydration causes carbonization and aromatization of the biomass. In this case, biochar formation is limited at low temperatures. The factor that provides high carbon yield is low temperature because less volatile components are removed from the structure at low temperatures [51]. When the temperature increases, much larger-molecule compounds decompose into small-molecule compounds, and more volatile components are removed from the structure. This situation caused the carbonization efficiency to decrease with the increase in carbonization temperature.

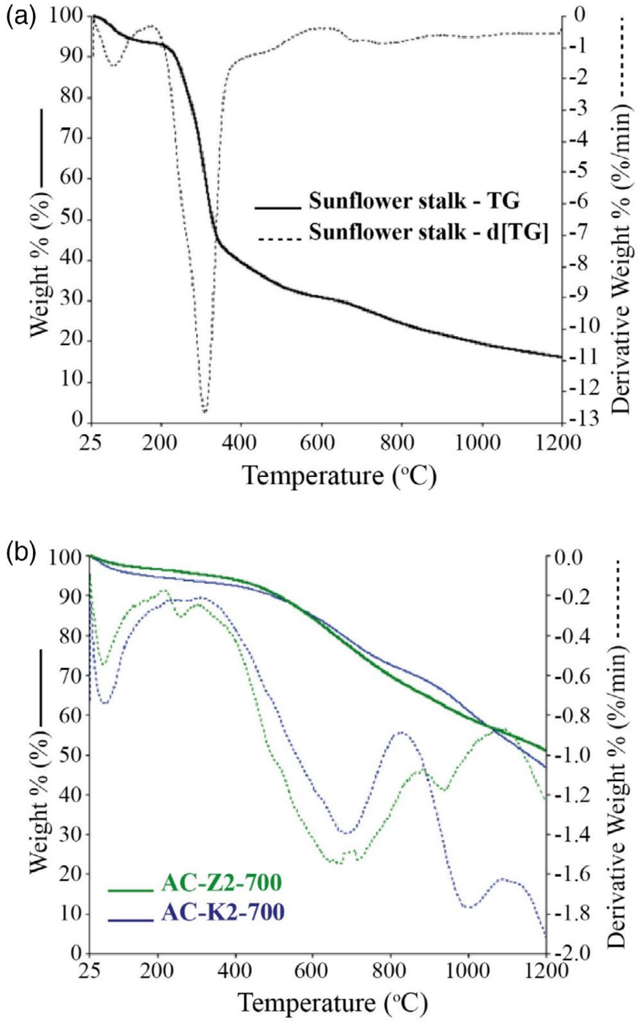

FIGURE 5 | The TG and d[TG] thermograms of (a) sunflower stalk and (b) activated carbons.

3.1.4 | SEM/EDX Analysis

SEM technique shows the morphological surface and porous structure of sunflower stalk and ACs obtained by chemical activation methods using different carbonization temperatures and different activation agents $ZnCl_2$ and KOH [52]. Figures 6 and 7 show SEM images of sunflower stalk and ACs synthesized with $ZnCl_2$ and KOH. It is clear from the SEM images that the surface of the sunflower stalk has a non-porous structure at 5000× magnification and there are some occasional cracks on its surface. When the surface morphologies of the ACs were examined, it was seen that there were abundant pores formed by the activating agents during carbonization, and this shows that there was a significant difference in the morphological surface of the ACs compared to the raw material [53, 54]. SEM micrographs of ACs activated with $ZnCl_2$ and KOH were viewed at 1000× and 5000× magnification levels, respectively, and these magnification levels are relatively low to view mesopores or micropores, as can be understood from the scales in the images; these visible pores are macropores above 100 nm [40, 42]. However, large pores or macropores are quite evident in all samples and it is very clear that the pore structure of ACs activated with $ZnCl_2$ and KOH is different from each other. These results revealed that activating agents affect the topographic properties of carbon surfaces. The use of $ZnCl_2$ and KOH as chemical activating agents in

TABLE 2 | Thermogravimetric data calculated from DTA/TG analyzes of sunflower stalk and optimized activated carbons (T_{max} represents the maximum decomposition temperature, and ΔY the percentage weigh loss).

Samples	T_{max1}	ΔY_1	T_{max2}	ΔY_2	T_{max3}	ΔY_3	T_{max4}	ΔY_4	Residue (wt%) at 1200°C
Sunflower stalk	79.1	6.7	301.1	62.0	749.0	14.0	—	—	16.0
AC-K2-700	62.6	5.8	671.7	22.4	943.4	24.9	—	—	46.7
AC-Z2-700	61.6	2.6	255.6	1.6	677.3	34.0	898.5	14.5	50.9

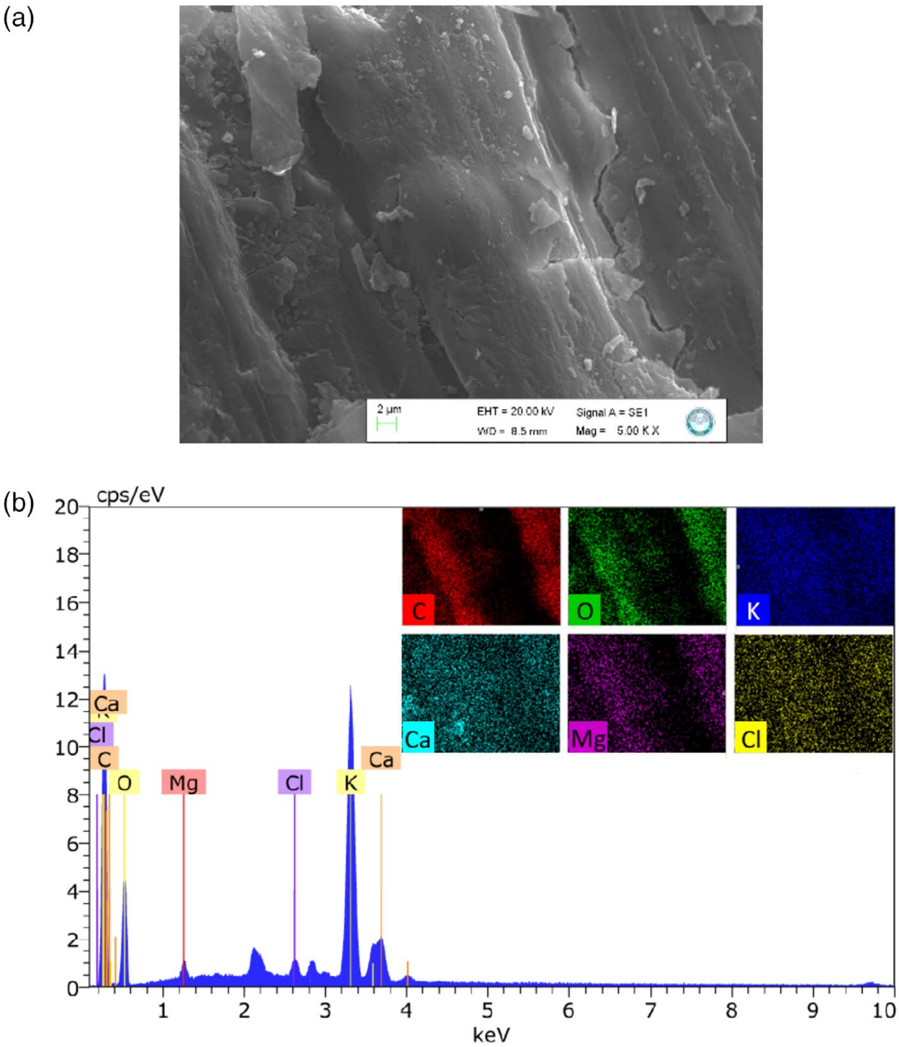

FIGURE 6 | (a) SEM images and (b) EDX spectrum/mapping of sunflower stalks.

AC production leads to distinct morphological differences due to their unique activation mechanisms. While KOH tends to produce AC with a smaller porous structure, $ZnCl_2$ generally results in a larger and heterogeneous porous structure. These differences are attributed to chemical interactions and physical changes caused by each activator during the activation process. The activation mechanism of KOH is more complex, and the structure can result in an explosive-style fragmentation after intercalation and even some gasification by hydroxide oxygen molecules. $ZnCl_2$, on the other hand, can remove H_2O molecules from the lignocellulosic structure of the raw material [55]. In the literature, it has been reported that ACs with a distinct surface morphology characterized by a decrease in surface area and pore volume with increasing activation temperature are obtained with $ZnCl_2$ activation [56]. On the other hand, it has been reported that KOH activation leads to high surface area and well-developed porous structure in ACs [57]. In other words, KOH activation tends to produce a well-developed porous structure, while $ZnCl_2$ activation results in a different morphological pattern. These differences are very important for applications such as adsorption and energy storage. SEM analysis of $ZnCl_2$-activated salak wedi bark shows a different pore distribution, fewer and less evenly distributed pores, compared to KOH [58].

When Figure 7 is examined, it is seen that in the AC-Z2-600 activated with $ZnCl_2$ at a ratio of 2:1, carbonization did not occur completely due to the low temperature and pore formation was limited. It is thought that when the temperature was increased, more pronounced pores were formed at 700°C and the structure became more porous due to the dehydration effect of $ZnCl_2$. When the carbonization temperature was increased to 800°C, enlarged pores and fragmentation were seen in the structure; at 900°C, structural collapses and collapsed pores in some areas were observed at extremely high temperatures. When the agent ratio was increased to 3:1, it was seen that the use of excess $ZnCl_2$ caused excessive pore growth. When Figure 7 is examined, it is seen that limited activation occurred in the AC-K2-600 activated with KOH at a ratio of 2:1 and some small pores started to form. At 700°C, homogeneously distributed pores became more prominent and the surface became rougher due to the strong activation effect of KOH. When the temperature increased to 800°C, larger pores were formed and there were fragments on the surface in some

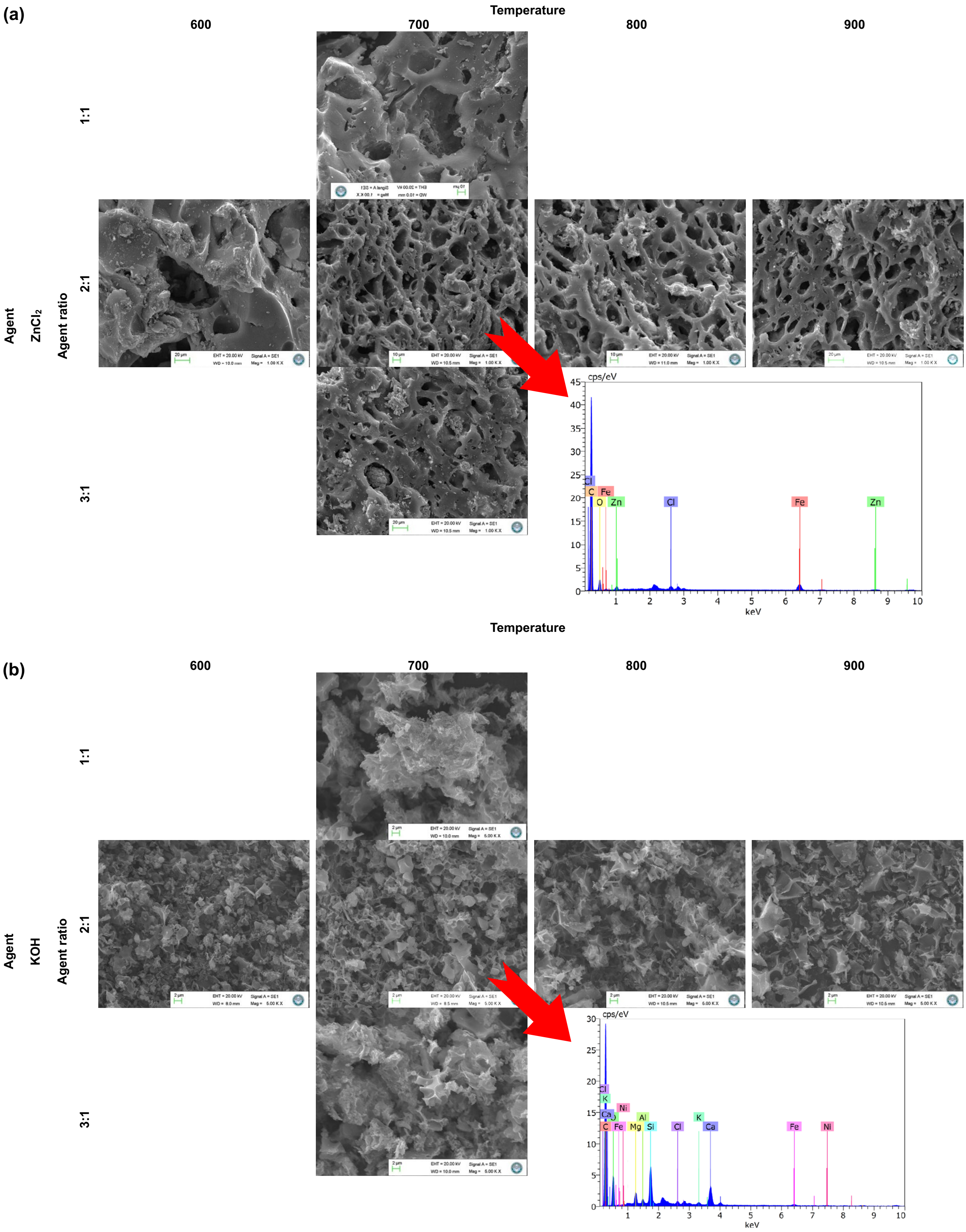

FIGURE 7 | SEM images of activated carbons produced from sunflower stalks at different activation temperatures with (a) $ZnCl_2$ and (b) KOH activations.

TABLE 3 | Elemental composition and distribution of sunflower stalk biomass and selected activated carbon samples.

Samples	C	O	K	Ca	Mg	Cl
Sunflower stalk	39.30	35.51	19.40	3.79	0.97	1.02
AC-Z2-700	79.11	13.03	—	—	—	—
AC-K2-700	64.11	24.58	—	—	—	—

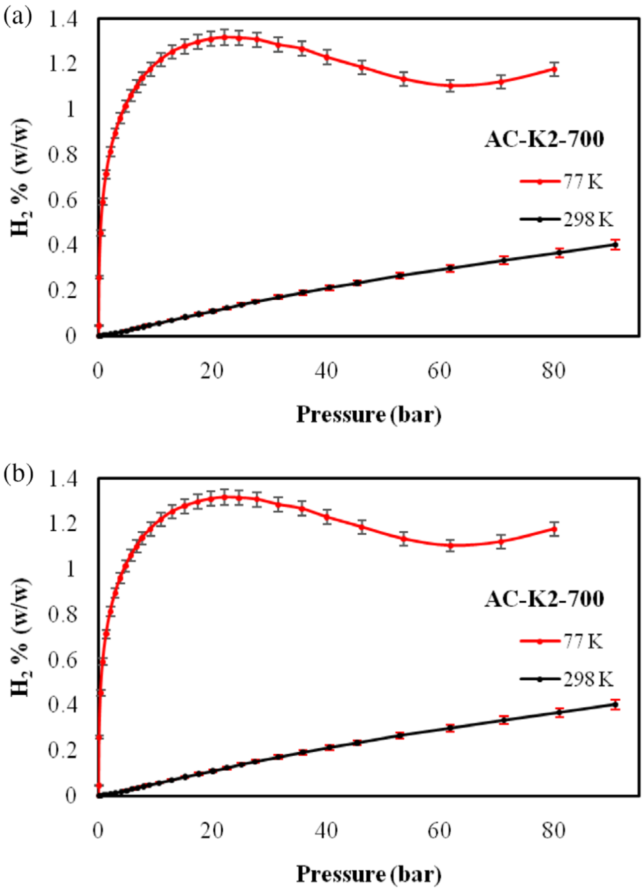

FIGURE 8 | Hydrogen storage capacities of (a) AC-Z2-700 and (b) AC-K2-700 at 298 and 77 K.

areas. At 900°C, it was observed that pores collapsed in some areas due to excessive temperature. Since KOH has a more aggressive activation mechanism than $ZnCl_2$, structural deterioration can occur faster at high temperatures and temperatures of 800°C and above can cause excessive pore growth or surface collapse in some areas. In the SEM images of ACs produced with both activating agents, the best pore structure was observed at 700°C and the activation of the activating agent at a ratio of 2:1 is generally optimum.

The elemental composition of sunflower stalk and optimized ACs was determined by energy dispersive X-ray microanalysis (EDX) and the results are given in Table 3. The elemental content of sunflower stalk contains 39.30% carbon and 35.51% oxygen. This relatively high oxygen content belongs to the oxygenated components of biomass such as cellulose, hemicellulose, and lignin. In addition, 19.40% potassium, 3.79% calcium, 1.02% chlorine, and 0.97% magnesium detected indicate the presence of elements that can exist in biomass. As shown in Figure 6, the presence of carbon and oxygen was detected in the EDX spectra of ACs. The carbon percentage of the optimized AC-Z2-700 increased significantly to 79.11%, while the amount of oxygen decreased to 13.03%. This shows that $ZnCl_2$ increased the carbon content by removing oxygenated components during carbonization. In the AC-K2-700, 64.11% C and 24.58% O were found, and it was understood that this sample contained slightly more oxygen compared to the $ZnCl_2$ activation. This indicates that the activation mechanism is different. As a result, EDX results showed that oxygenated components decreased and the amount of carbon increased with activation, which proves that carbonization was successful. Moreover, spectral analysis revealed the presence of trace concentrations of activating agents in ACs that were not eliminated during the washing process.

The EDX analysis revealed a significantly higher C/O ratio for AC-Z2-700 compared to AC-K2-700. This difference in elemental composition suggests variations in the surface chemistry and porosity that are related to the activation process. The significant difference in carbon/oxygen content observed between AC-Z2-700 and AC-K2-700 can be attributed to the distinct activation mechanisms of $ZnCl_2$ and KOH. $ZnCl_2$ activation proceeds primarily via a dehydration mechanism, where $ZnCl_2$ acts as a Lewis acid to promote dehydration of the carbon precursor, facilitating cross-linking and aromatization reactions. This process reduces the formation of oxygen-containing surface functional groups, leading to a higher carbon content and lower oxygen content in the final product. In contrast, KOH activation involves an etching mechanism, where KOH reacts with carbon at elevated temperatures to produce metallic potassium, potassium carbonate, and potassium oxide. These species intercalate into the carbon lattice and create additional porosity but also introduce and retain more oxygen-containing functionalities on the surface. Consequently, the different chemical pathways explain the higher oxygen content in AC-K2-700 compared to AC-Z2-700, as reported in previous studies on chemical activation with $ZnCl_2$ and KOH [59, 60]. To remove activating agent residues, repeated washing with 0.1 M HCl followed by deionized water was performed. The residual levels detected by EDX are too low to significantly affect the structural stability or hydrogen adsorption performance of the materials. The use of higher-concentration acid was avoided, as it could lead to excessive dissolution of the carbon framework or pore collapse. Furthermore, repeated hydrogen adsorption–desorption cycling tests confirmed that these residuals do not negatively influence the reproducibility or stability of the storage capacity.

3.2 | Hydrogen Storage

As a result of BET surface area and pore volume optimization, the hydrogen storage capacities of AC-Z2-700 and AC-K2-700 were investigated in a wide pressure range at room and cryogenic temperatures. Figure 8 shows the amount of hydrogen stored against pressure at room temperature for AC-Z2-700 and AC-K2-700. The amount of hydrogen adsorbed on both ACs at room temperature increases in direct proportion to the pressure. This situation can often be explained by Henry's

Law. Henry's Law states that the adsorption of a gas onto a solid surface is proportional to the pressure of the gas and the proportionality constant is the Henry constant. Increased pressure increases the probability of hydrogen molecules hitting the surface. This affects the balance between adsorption and desorption. According to Henry's Law, under high pressure, the adsorption rate is greater than the desorption rate, which leads to more hydrogen binding to the surface. At the same time, as the pressure increases, the density of the gas also increases. Higher density means that more hydrogen molecules are present in a certain volume. This states that more hydrogen reaches the adsorbent surface and is retained there [61]. A similar situation was observed for the adsorption of hydrogen on NaA zeolites at 77 and 300 K. The study revealed that the Henry's Law constant for hydrogen adsorption on NaA zeolites varied with temperature, and there was a linear relationship between hydrogen removal and inlet pressure at low loading conditions [62]. In another study, Henry's Law was successfully applied to describe the adsorption of hydrogen onto AC samples. In the measurements made at 273 and 298 K, the dependence of the adsorbed hydrogen amount on the equilibrium pressure showed a linear relationship. In particular, the Henry coefficient reached the highest values for the RMS-AC sample, which indicated that the adsorption capacity of hydrogen was higher than the others [22]. Again, the curve shows that the hydrogen storage capacity of AC-Z2-700 at room temperature is higher than that of AC-K2-700. The hydrogen storage capacity of the adsorbents is greatly affected by the BET surface area and pore volume, especially the micropore volume. From Table 1, it is seen that the BET surface area of AC-K2-700 is lower than that of AC-Z2-700. The surface area determines how much gas molecules can interact with the surface. Since AC-Z2-700 has a higher surface area, it can be said that there will be more active points on its surfaces and as a result, more hydrogen molecules will be adsorbed on its surfaces. Therefore, its storage capacity is higher. Another parameter affecting the hydrogen storage capacity is the pore volume. From Table 1, it is seen that both samples have a microporous structure and that the micropore volume of AC-Z2-700 is higher. Micropores are pores that generally have diameters smaller than 2 nm. Such pores offer a large surface area for the adsorption of hydrogen molecules. Materials with a high micropore volume allow more hydrogen molecules to be stored, which increases the storage capacity. At 298 K and 20 bar, the hydrogen storage capacity of AC-K2-700 was calculated as 0.11 wt%, while the storage capacity of AC-Z2-700 was calculated as 0.15 wt%. In the literature, it was determined that the AC produced as a result of zinc chloride activation of tangerine peel had a higher hydrogen storage capacity than the AC produced by potassium hydroxide activation. Activation with $ZnCl_2$ provided higher surface areas and porosity, allowing more hydrogen to be adsorbed. Although ACs produced by KOH activation had the advantage of microporosity, they generally reached a lower hydrogen storage capacity [21].

The hydrogen adsorption behaviors at cryogenic temperature largely depend on the physical adsorption mechanism caused by the textural properties of the adsorbent materials. Especially for microporous carbon materials, hydrogen removal is dominant in the micropore volume and pore size [63]. The isotherm curves at room and cryogenic temperatures are different from each other. At cryogenic temperature, the stored amount increases rapidly with increasing pressure at the beginning, and when the pressure continues to increase, the stored amount decreases after the maximum point without a plateau. The decrease in the stored amount of hydrogen after a certain pressure value can be explained by the excess adsorption behavior. Excess adsorption is a process that refers to the accumulation of a gas or liquid on a solid surface in a higher amount than that of the gas in the liquid. This mechanism generally occurs under high pressure and low temperature conditions and is related to the tendency of the adsorbed substance to remain on the surface. During excessive adsorption, hydrogen molecules bind strongly to the AC pores, causing concentration in the pores [22]. It is observed that when the pressure is continued to be increased after the excessive adsorption event, the storage capacities of the samples start to increase again. This secondary increase in storage capacity after the apparent saturation point can be attributed to the gradual filling of ultramicropores and the possible compression-induced densification of adsorbed hydrogen layers within the pore network at higher pressures. As the applied pressure continues to rise, hydrogen molecules may penetrate into narrower pores that were initially less accessible due to kinetic limitations, or additional adsorption layers may form through enhanced van der Waals interactions. Similar behaviors have been reported in high-pressure adsorption studies, where multi-layer adsorption and pore wall interactions become more significant beyond the initial saturation stage. In the literature, AC samples produced from agricultural waste materials such as red mombin seeds, cocoa shells, mango seed outer parts, and coffee pulp exhibited similar behaviors at around 10 bar at 77 K [22] and ACs produced from tangerine peel using different activation methods exhibited similar behaviors in the range of 10–15 bar at cryogenic temperature [21].

As can be seen from the figures, the hydrogen storage capacities of ACs at cryogenic temperatures are higher than those at room temperature. The hydrogen storage capacities of AC-Z2-700 and AC-K2-700 at 20 bar and 298 K are 0.15 and 0.11 wt%, while at 77 K they are 2.39 and 1.31 wt%, respectively. These results are also in good agreement with Chahine's rule. This rule is accepted as a reference value for carbon materials at cryogenic temperatures and establishes a relationship between surface area and hydrogen storage capacity. According to this rule, approximately 2 wt% hydrogen storage capacity is expected per 1000 m^2/g surface area [64]. This means that the hydrogen storage capacity will increase with increasing surface area. The results obtained are consistent with the expected theoretical value for the adsorption of hydrogen in the $\sqrt{3}$ configuration on double-sided graphene sheets [65]. Activated carbon obtained from horse chestnut by activation of $ZnCl_2$ at 600°C has a storage capacity of 1.48 wt% at 298 K, while it has a storage capacity of 4.46 wt% at 77 K. In another study, the hydrogen storage capacities of ACs produced by activation of $ZnCl_2$ and KOH from tangerine peel were calculated as 0.14 wt% and 0.10 wt% at approximately 20 bar and 298 K, respectively, while they were 1.7 and 1.25 wt% at 77 K. The reason for the higher hydrogen storage capacity at 77 K (approximately −196°C) is that lower temperatures reduce the kinetic energy of gas molecules, thereby minimizing the probability of desorption and significantly enhancing the effectiveness of

TABLE 4 | Hydrogen storage capacities of some activated carbon samples at 77 K.

Activated carbon sources	Pressure (bar)	H_2 wt%	References
Rich-coal fly ash	1	1.35	[66]
Tangerine peel	20	1.70	[21]
Tangerine peel	20	1.22	[21]
Almond shells	25	2.53	[16]
Rice husks	1	2.85	[63]
Chestnut shell	30	4.46	[18]
Olive pomace	25	2.59	[67]
Tamarind seeds	20	1.97	[68]
Sunflower stalk (AC-Z2-700)	30	2.55	In this study
Sunflower stalk (AC-K2-700)	24	1.34	In this study

van der Waals interactions. At this temperature, the overlap of potential energy fields within the micropores strengthens the adsorptive forces, while the increased gas-phase density raises the probability of hydrogen molecules colliding with the pore walls, thus maximizing adsorption likelihood. The synergistic effect of reduced thermal mobility and increased potential field overlap constitutes the primary mechanism for the markedly higher hydrogen storage capacity observed in ACs at 77 K compared to room temperature. In addition, physical adsorption mechanisms become more effective at lower temperatures, which helps more gas to penetrate into the pores of ACs. As a result, the energy required to store hydrogen at 77 K decreases, leading to higher storage capacities.

It is stated in the literature that the hydrogen storage capacities of ACs vary depending on the plant material used in AC production, production method, chemical agent, and measurement conditions. Table 4 summarizes the hydrogen storage capacities of various ACs at 77 K under different pressures. Reported values span a wide range due to variations in biomass precursors, activation protocols, and measurement conditions. For instance, rich-coal fly ash exhibits 1.35 wt% at 1 bar [66], while tangerine peel–derived carbons yield 1.70 and 1.22 wt% at 20 bar [21]. Almond shells show 2.53 wt% at 25 bar [16], and rice husks present a notable 2.85 wt% at 1 bar [63], demonstrating that effective storage is possible even under low pressure. At higher pressures, capacities generally increase; chestnut shell carbons reach 4.46 wt% at 30 bar [18], olive pomace yields 2.59 wt% at 25 bar [67], and tamarind seeds show 1.97 wt% at 20 bar [68]. In the present work, sunflower stalk–derived AC-Z2-700 achieved 2.55 wt% at 30 bar, while AC-K2-700 recorded 1.34 wt% at 24 bar. Although absolute values cannot be directly compared due to methodological differences, these results demonstrate that sunflower stalk carbons are competitive withand in some cases superior to, other biomass-derived carbons with similar surface characteristics. Notably, AC-Z2-700 reached 1.92 wt% at 77 K and 10 bar, matching or exceeding values reported for almond shells (1.65 wt%) and tangerine peel (1.72 wt%) under comparable conditions. While certain precursors such as peanut shells have shown slightly higher capacities (~2.05 wt%), these typically require harsher activation temperatures or compromise carbon yield.

The favorable performance of sunflower stalk carbons arises from their high micropore volume, narrow pore size distribution, and low oxygen content, which enhance hydrogen adsorption efficiency at cryogenic temperatures. Additionally, their hydrogen uptake at 298 K falls within the upper range for biomass-based carbons, underscoring their suitability for practical applications. These attributes position sunflower stalk–derived ACs as sustainable, high-performance candidates for hydrogen storage, offering a competitive balance of capacity, precursor availability, and production efficiency.

3.3 | Adsorption Isotherms

Adsorption isotherms are mathematical relations that describe the concentration of molecules adsorbed on an adsorbent surface and the interaction of these molecules with the surface. The most commonly used isotherms to study the adsorption process from the gas phase to the solid surface are the Freundlich, Langmuir, Dual-Langmuir, Temkin, and Henry isotherms.

The Freundlich isotherm is an empirical formula used to model adsorption processes on heterogeneous surfaces. The mathematical expression of the Freundlich isotherm is as follows:

$$n = K_F P^{1/n_F} \tag{1}$$

In linear form,

$$\ln(n) = \ln K_F + \frac{1}{n_F} \ln P \tag{2}$$

Here, n is the adsorption amount at P pressure (mmol/g); K_F and n_F are constants specific to the Freundlich isotherm; K_F represents the adsorption capacity and n_F represents the intensity of adsorption processes. If the experimental data are compatible with the Freundlich isotherm, the extrapolation of the curve of $\ln(n)$ against $\ln P$ should give a straight line with $\ln K_F$ and a slope of $1/n_F$. The n_F and K_F values are calculated from the slope and extrapolation. One of the basic features of this model is that if the n_F value is greater than 1, it indicates that the adsorption capacity of the system increases, while if the n_F value is less than 1, it indicates a lower adsorption capacity. The Freundlich isotherm is commonly used in various applications for adsorbents with heterogeneous surfaces in cases where adsorbate–adsorbent interactions are relatively weak. This is because the Freundlich model can account for the presence of adsorption sites with different energies and for multilayer adsorption [69].

The Langmuir isotherm is a model developed to describe adsorption processes on homogeneous surfaces. The Langmuir isotherm is a frequently used tool for characterizing adsorption processes and is important in many areas for the analysis of adsorption data. The mathematical expression of the Langmuir isotherm is as follows:

$$\frac{P}{n} = \frac{1}{K_1 n_{m1}} + \frac{P}{n_{m1}} \tag{3}$$

where n is the density of adsorption at a pressure of P, n_{m1} is the saturated adsorption value, and K_1 is an equilibrium coefficient. According to this equation, the plot of P/n against P should give a straight line with slope $1/n_{m1}$ and extrapolation $1/n_{m1}K_1$ [70]. Similarly, a dual Langmuir equation, where each hydrogen molecule dissociates and occupies two sites, can be given as follows:

$$\frac{P^{1/2}}{n} = \frac{1}{K_2 n_{m2}} + \frac{P^{1/2}}{n_{m2}} \tag{4}$$

Note that the monolayer capacity n_{m2} and equilibrium coefficient K_2 have different numerical values in the Equations (3) and (4) and thus have been, respectively, subscripted [16].

Temkin isotherm is a model used to explain adsorption processes and is preferred especially in cases where the interaction between the adsorbate and the adsorbent is important. This model is based on the fact that the interactions of molecules on the surface increase with the increase of the adsorption temperature. Mathematically, Temkin isotherm is expressed by the following formula:

$$n = A \ln P + B \tag{5}$$

here n is the adsorption amount at pressure P (mmol/g); A and B are constants specific to the Temkin model; A represents the adsorption capacity and B represents the term related to the heat dependent on temperature. According to the Temkin model, the curve of n against $\ln P$ should give a straight line with slope A and extrapolation B [16].

Henry Law states that the adsorption of a gas on a solid surface is proportional to its pressure in the gas phase. This law is especially valid under low pressure conditions and is widely used in understanding the behavior of gases on solid surfaces. The mathematical expression of Henry Law is as follows:

$$n = K_H P \tag{6}$$

here n is the amount of adsorption at pressure P; K_H is the Henry coefficient; and P is the pressure of the gas. According to this equation, the curve of n against P should give a straight line with a slope of K_H passing through the origin [62].

Table 5 shows the regression coefficient values and the corresponding isotherm constant values for different isotherm equations. As explained in the hydrogen storage analysis section, the ACs exhibit different behaviors at different temperatures. The experimental data exhibited a linear relationship with pressure at room temperature, while excessive adsorption behavior was observed at cryogenic temperature. It is seen from the table that the regression coefficients at room and cryogenic temperatures are also different. The regression coefficients calculated at room temperature from Freundlich, Langmuir, Dual-Langmuir, Temkin, and Henry equations for AC-Z2-700 and AC-K2-700 are 0.9954 and 0.9804, 0.0383 and 0.0370, 0.2915 and 0.2651, 0.6265 and 0.6543, and 0.9913 and 0.9914, respectively. These results show that the experimental data at room temperature are in good agreement with the Freundlich and Henry equations due to the high regression coefficient values. From Table 5, the n_F values for AC-Z2-700 and AC-K2-700 are 0.93 and 0.92, respectively. These values are less than one, indicating that the storage capacity of the adsorbents is also low. At cryogenic temperature, the regression coefficients calculated from Freundlich, Langmuir, Dual-Langmuir, Temkin, and Henry equations for AC-Z2-700 and AC-K2-700 are 0.9266 and 0.9431, 0.9977 and 0.9959, 0.9217 and 0.9739, 0.9552 and 0.9613, and 0.5964 and 0.6438, respectively. According to these results, the isotherm with the highest regression coefficient is the Langmuir isotherm. Another parameter that shows that the experimental data at cryogenic temperature are in good agreement with the Langmuir isotherm is the fact that the experimental and computational n values are in good agreement with each other. For samples AC-Z2-700 and AC-K2-700, $n_{(exp)}$ values are 1.254 and 0.635 µmol/g, while n_m values are 1.300 and 0.658 µmol/g, respectively. These data show that the adsorption dynamics of hydrogen gas change depending on temperature and each model is more successful in certain temperature ranges. In the literature, hydrogen adsorption isotherm analyses of ACs produced from almond shells were investigated with Langmuir, Temkin, and Freundlich isotherms. The obtained data showed that the Freundlich isotherm provided the best agreement with the experimental results. The maximum hydrogen adsorption values calculated according to the Langmuir model did not agree with the experimental values. This showed that the active sites on the AC surface were not homogeneous and the adsorption was not monolayered. Isotherm analyses revealed the physical adsorption properties of hydrogen and the importance of adsorption temperature and pressure conditions [15]. Different isotherm models for hydrogen adsorption were compared in terms of their agreement with the experimental data and the accuracy

TABLE 5 | Isotherm and regression coefficient values.

		Langmuir					Freundlich				
Samples	**T (K)**	**$n_{(exp)}$**	**n_m**	**K_1**	**R^2**	**Dual Langmuir R^2**	**n_F**	**K_F**	**R^2**	**Temkin R^2**	**Henry R^2**
AC-Z2-700	77	1.254	1.300	0.648	0.9977	0.9217	2.599	0.420	0.9266	0.9552	0.5964
	298	—	—	—	0.0383	0.2915	0.928	0.003	0.9954	0.6265	0.9913
AC-K2-700	77	0.635	0.658	0.889	0.9959	0.9739	2.733	0.259	0.9431	0.9613	0.6438
	298	—	—	—	0.0370	0.2651	0.920	0.002	0.9804	0.6543	0.9914

of the parameters they estimated. In particular, it was determined that the Langmuir model exhibited poor performance at high pressures, while models such as Levenberg–Marquardt, Toth, and Unilan gave better results [71]. The adsorption data of hydrogen at the Pd–SiO_2 interface were found to be in good agreement with the Temkin isotherm. The suitability of the Temkin isotherm for describing hydrogen adsorption at the Pd–SiO_2 interface arises from its assumption that the adsorption energy varies with surface coverage. The model predicts that adsorption initially occurs at high-energy sites, and as the hydrogen concentration increases, the adsorption energy gradually decreases. This behavior indicates that hydrogen binds to active sites with different energies at the Pd–SiO_2 interface and that the surface electrostatic potential and charge distribution influence this process. The experimental data showed good agreement with both the maximum hydrogen concentration and the practical upper limit predicted by the Temkin model. This agreement demonstrates that electrostatic interactions play a dominant role in the adsorption process and that the energy distribution within the system is a determining factor for hydrogen retention [72].

3.4 | Adsorption Rate and Kinetics

Studies on hydrogen adsorption show that pore size significantly affects the adsorption behavior, with the highest capacity being observed at 0.7 nm pore size. It has been shown that adsorption rates vary between microporous and mesoporous materials, and that there is a linear relationship between adsorption capacity and specific surface area [73]. Carbon-based adsorbents are promising for hydrogen storage [74]. Figure 9 shows the change in the stored amount of hydrogen with time for AC-Z2-700 and AC-K2-700. Experiments were carried out at 10, 30, and 40 bar pressures at cryogenic temperature. It is seen that the adsorption process for both ACs is fast and reaches dynamic equilibrium within 2 min. The initial rapid adsorption is due to the empty active sites on the AC surface and pores. As these high-energy sites become occupied by hydrogen molecules, fewer vacant sites remain, and adsorption progressively shifts to less favorable regions. This results in a decrease in the covering fraction and a slowdown in the adsorption rate until equilibrium is reached.

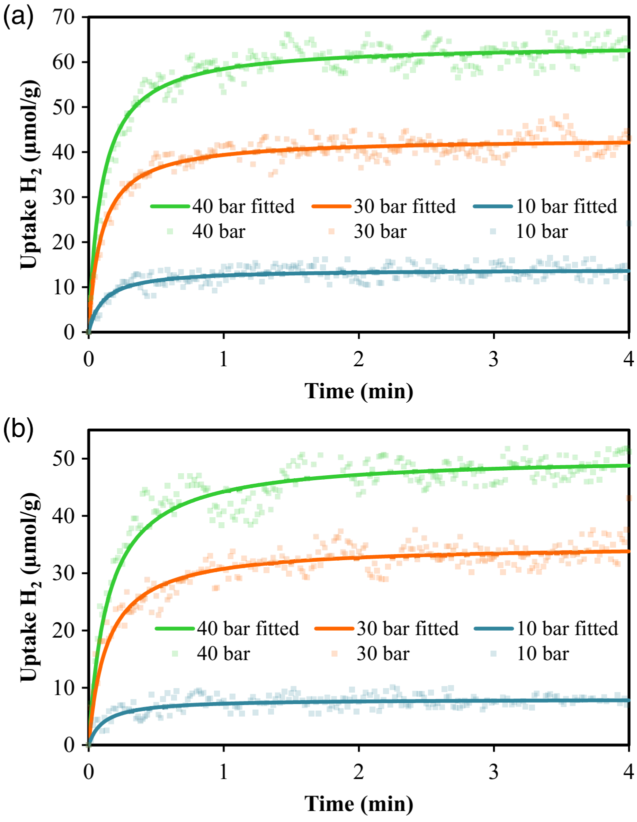

FIGURE 9 | The changing of hydrogen storage capacities with time of (a) AC-Z2-700 and (b) AC-K2-700 at different pressures.

Since the adsorption process involves mass transfer of adsorbate from any phase to the solid surface, the investigation of adsorption kinetics and mechanism is very important in terms of process efficiency. Different methods have been used in the literature for the analysis of adsorption kinetic data. In this study, the adsorption kinetic data on the surface and pores of AC were analyzed by pseudo first order, pseudo second order, mass transfer, and intraparticle diffusion methods. The method that best fits the experimental data was determined according to the linear regression correlation coefficient value and equation parameters. The pseudo-first-order model is generally used for systems with low concentration and/or pressure and shows that adsorption is accelerated, that is, it depends on the interaction of the adsorbate with the surface or the rate of transfer from the bulk phase to the surface. This model is important for analyzing the behavior of the system before it reaches an equilibrium point. The pseudo-first-order kinetic equation describes the dynamics of an adsorption process and is usually expressed as:

$$\frac{dq_t}{dt} = k_1\left(q_e - q_t\right) \tag{7}$$

here q_t is the adsorbed amount of adsorbate at any time t (μmol/g); t is time (min); k_1 is the pseudo first order rate constant (min^{-1}); q_e is the amount of adsorbate adsorbed at equilibrium (μmol/g). When we integrate this equation and apply the initial conditions, we arrive at the following form:

$$\ln\left(q_e - q_t\right) = \ln q_e - k_1 t \tag{8}$$

If the experimental data agree with this equation, the plot of $\ln(q_e - q_t)$ against t should give a straight line. The value of k_1 can be calculated from the slope and the value of q_e from the extrapolation value. In this equation, q_t describes a logarithmic relationship as it approaches the value of q_e as time increases.

The pseudo-second order model is generally applicable to systems with high concentration and/or pressure and usually describes chemical adsorption processes. This model suggests that chemical bonds are formed in the adsorption process and that the interaction between the adsorbate and the adsorbent is important. The pseudo-second order kinetic equation is a widely used model to describe adsorption processes. This equation is as follows:

$$\frac{dq_t}{dt} = k_2\left(q_e - q_t\right)^2 \tag{9}$$

here q_t is the amount adsorbed at any time t (μmol/g); t is time (min); k_2 is the pseudo second order rate constant (g/(μmol min));

q_e is the amount adsorbed at equilibrium (μmol/g). The integrated form of this equation is as follows:

$$\frac{1}{(q_e - q_t)} = k_2 t + \frac{1}{q_e} \tag{10}$$

If this equation is rearranged as follows:

$$\frac{t}{q_t} = \frac{1}{k_2 q_e^2} + \frac{t}{q_e} \tag{11}$$

If the experimental data are compatible with this equation, the curve of t/q_t versus t presents a linear relationship. q_e and k_2 are calculated from the slope and extrapolation. Figure 10 gives the plots of t/q_t versus t for AC-Z2-700 and AC-K2-700. The regression coefficient values obtained by applying the experimental data obtained for the adsorption of hydrogen on the surface and pores of AC-Z2-700 and AC-K2-700 to the pseudo first and second order kinetic equations are given in Table 6. The regression coefficient (R^2) values for the pseudo-first-order kinetic equation were found to be in the range of 0.1406–0.5751, which are considerably lower than the acceptable threshold for a good fit (generally $R^2 > 0.90$). In contrast, the R^2 values for the pseudo-second-order kinetic equation were much higher, in the range of 0.9434–0.9937. This clear difference indicates that the pseudo-first-order model does not adequately describe the hydrogen adsorption kinetics of the studied ACs, whereas the experimental data show strong compatibility with the pseudo-second-order kinetic model. Such behavior suggests that the adsorption process is more likely governed by chemisorption or a combination of rate-limiting steps involving surface heterogeneity and pore diffusion, rather than a simple physisorption-controlled mechanism. Another parameter showing that the experimental data are compatible with the pseudo second order kinetic equation is the agreement of the experimental $q_{e(exp)}$ and computational $q_{e(cal)}$ values. Since both the regression coefficient is high and the experimental $q_{e(exp)}$ and computational $q_{e(cal)}$ values are compatible with each other, it can be said that the pseudo second-order kinetic equation is a good fit with the experimental data. The adsorption rate constants of hydrogen on the AC decrease with increasing pressure. This shows that the adsorption of hydrogen on the AC occurs quite rapidly at low pressures. However, it is noteworthy that the rate constant decreases as the pressure increases. This indicates that the AC surface and pores are covered with hydrogen molecules at the beginning or at low pressures. At high pressures, the rate constant decreases due to the decrease in the number of sites where hydrogen molecules can be adsorbed or the decrease in the coverage fraction. As a result, while the adsorption of hydrogen on AC is more efficient at low pressures due to the preferential filling of high-energy adsorption sites within the micropores via strong van der Waals interactions, the performance decreases at high pressures as these sites become saturated and adsorption shifts to lower-energy surfaces. This information provides important parameters to be considered in the design of hydrogen storage and utilization systems.

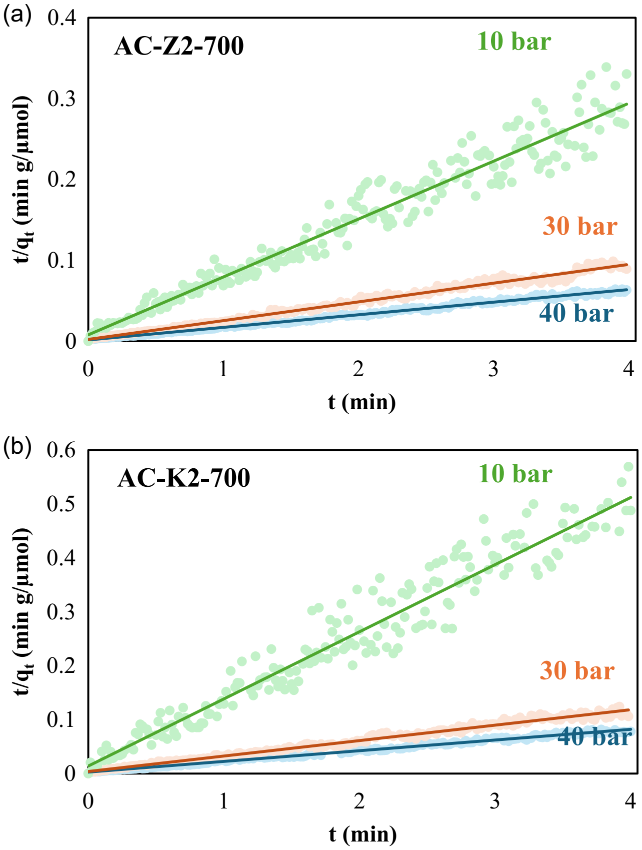

FIGURE 10 | The plots of t/q_t versus t for (a) AC-Z2-700 and (b) AC-K2-700.

TABLE 6 | The kinetic parameters for the adsorption of hydrogen on AC-Z2-700 and AC-K2-700.

			Pseudo-second order					Weber–Morris			
Samples	**Pressures (bar)**	**Pseudo-first order R^2**	**R^2**	**$q_{e(exp)}$ (μmol/g)**	**$q_{e(cal)}$ (μmol/g)**	**k_2**	**Boyd R^2**	**R^2_1**	**k_1**	**R^2_2**	**k_2**
AC-Z2-700	40	0.4496	0.9937	67.6	64.1	0.162	0.3566	0.9746	84.11	0.3240	4.76
	30	0.4214	0.9874	49.5	43.1	0.244	0.3589	0.9655	59.45	0.2920	3.67
	10	0.2415	0.9525	17.5	14.0	0.649	0.2745	0.9565	22.47	0.1449	1.63
AC-K2-700	40	0.5751	0.9922	54.9	50.5	0.140	0.4408	0.9760	66.05	0.4836	5.95
	30	0.4374	0.9866	38.0	34.9	0.209	0.4626	0.8754	40.21	0.4730	5.03
	10	0.1406	0.9434	12.1	8.1	1.107	0.1890	0.6418	9.80	0.0797	0.88

There are very limited studies in the literature investigating the adsorption kinetics and mechanism of hydrogen on solid adsorbents. Hydrogen gas adsorption kinetics were investigated on Pt/TiO_2/Pt structured sensors. It was found that the adsorption showed very good agreement with the pseudo-second-order model and this model exhibited a high correlation coefficient with the experimental results (higher than 0.99). This helped to understand the kinetic mechanism of hydrogen gas adsorption [75]. In another study, Matsumoto et al. investigated the hydrogen absorption kinetics of magnesium fibers under different temperature and pressure conditions using the Avrami equation to analyze the absorption behavior. They reported that the n values obtained from the Avrami equation were in the range of 0.7–1.3, indicating that the rate-determining step was diffusion. The authors noted that when the n value is close to 1, the rate-limiting step is generally interpreted as one-dimensional or pseudo-one-dimensional diffusion through micropores. This suggests that hydrogen molecules must diffuse through the complex pore network of the material before reaching the adsorption sites, and that diffusion resistance dominates the overall kinetic process. Furthermore, the study observed that the n value remained largely unchanged despite variations in temperature and pressure, implying that the pore structure and tortuosity were not significantly altered under the test conditions [76]. The effects of boron doping on enhancing the hydrogen storage capacity of boron carbon nanotubes (BCNTs) were investigated, and the kinetic analysis revealed that the hydrogen adsorption process follows the pseudo-second-order model. Interestingly, the highest hydrogen storage capacity was achieved at the lowest rate constant value. This inverse relationship can be attributed to the fact that boron doping increases both the number and binding strength of active sites, thereby enhancing the total storage capacity. However, stronger adsorption interactions and deeper potential wells tend to slow the adsorption kinetics, as hydrogen molecules require more time to diffuse into and occupy these energetically favorable sites. These findings indicate that the boron doping level is a critical factor influencing both the capacity and kinetics of hydrogen adsorption in BCNTs [77]. The colored symbols in Figure 9 show the experimentally measured storage capacity values. The curve shows the q_e and k_2 values calculated from the pseudo-second-order equation written in the Equation (11) and then the change of the calculated q_t values against different t values. It can be said that the fitting curve is in quite good agreement with the experimental data. This is another indication of the agreement of the pseudo-second-order equation with the experimental results.

An adsorption process generally occurs in three steps. The first is the mass transfer of the adsorbate to the boundary layer of the adsorbent. The second is the intraparticle diffusion of the adsorbate into the pores of the adsorbent, and the third is the adsorption of the adsorbate on the surface of the adsorbent [78]. The first and second steps are considered to be the main rate-controlling steps; the third step is assumed to be fast. From Figure 9, it is seen that the adsorption of hydrogen on the surface of the samples reaches dynamic equilibrium in about 2 min. Therefore, it can be said that the third step is not the rate-determining step. Diffusion models are based on the assumption that diffusion is the rate-determining step. The most commonly used models in the literature to elucidate the adsorption mechanism are the Boyd and Weber–Morris equations.

The Boyd equation is a model developed to describe the diffusion kinetics of adsorbate through a liquid film. This model, proposed by Boyd et al., has an important place in understanding the rate and mechanism of adsorption processes, as it helps determine whether the rate-controlling step is governed by external film diffusion or by intraparticle diffusion, thereby providing insight into the dominant mass transfer mechanism [79]. The Boyd equation is as follows:

$$\frac{dt}{dq} = R\left(q_t - q_e\right) \tag{12}$$

here q_t is the amount adsorbed at any time t (μmol/g); q_e is the amount adsorbed at equilibrium (μmol/g); and R is the external diffusion coefficient. If the above equation is integrated to the initial conditions $q_0 = 0$,

$$q_t = q_e\left(1 - e^{-Rt}\right) \tag{13}$$

If the logarithm of both sides of the Equation (13) is taken, the linear form of the Boyd equation is obtained.

$$\ln\left(1 - \frac{q_t}{q_e}\right) = -RT + A \tag{14}$$

This equation shows how the adsorption process develops with time, and the R value determines the rate of the external diffusion process. If the graph drawn based on the Boyd equation gives a straight line passing through the origin, this indicates that the situation is under intraparticle diffusion control.

The Weber-Morris model is an adsorption kinetic model developed to explain the intraparticle diffusion process. This model helps to understand the movement of the adsorbate within an adsorbent, that is, how it diffuses within the particle. The basic equation of the Weber-Morris model is as follows:

$$q_t = k_{int} t^{1/2} + C \tag{15}$$

here q_t is the adsorbed amount of adsorbate at any time t (μmol/g); k_{int} is the intraparticle diffusion rate constant (μmol/g min$^{0.5}$); t is time (min); and C is a constant representing the effect of diffusion within the particle. This model assumes that intraparticle diffusion is one of the most important stages in the adsorption process. The equation shows that q_t values increase proportionally with $t^{0.5}$ on a graph plotted with the square root of time. If this graph passes through the origin, this indicates that the process is controlled by intraparticle diffusion. In addition, the Weber–Morris model offers a different perspective than the Boyd equation and can evaluate the effects of other mechanisms such as surface phenomena in addition to intraparticle diffusion. In general, the Weber–Morris model is an important tool for understanding the dynamics of adsorption processes.

The parameters and regression coefficient values calculated by applying the experimental data to the Boyd and Weber–Morris

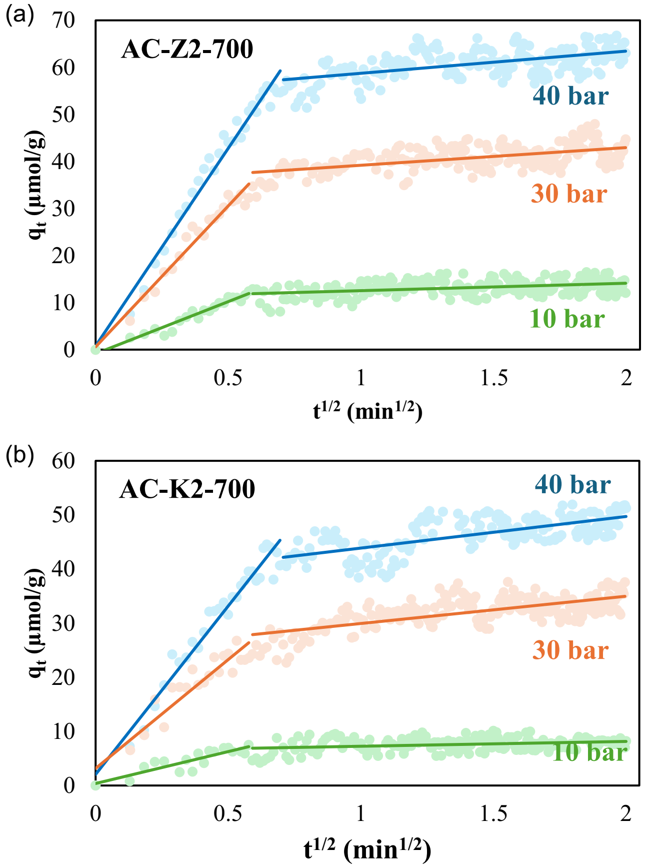

FIGURE 11 | The plots of q_t versus $t^{1/2}$ for (a) AC-Z2-700 and (b) AC-K2-700.

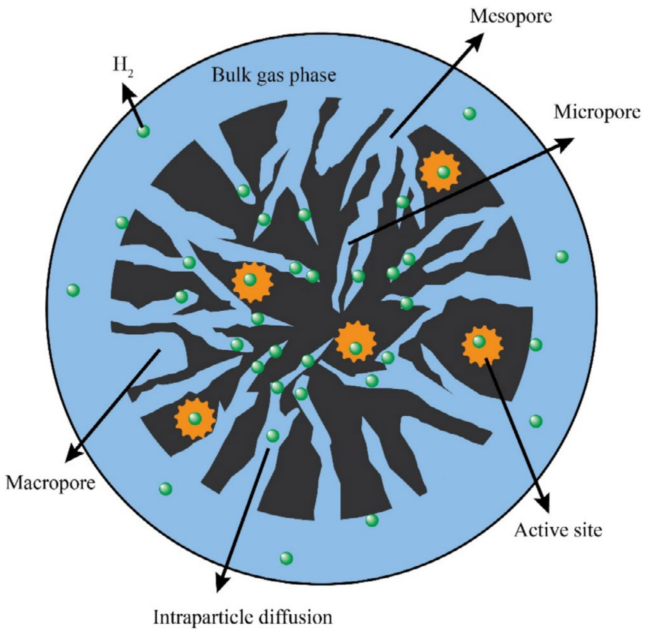

FIGURE 12 | Intraparticle diffusion mechanism of hydrogen into the pores of activated carbon.

equations are given in Table 6. It is observed that the R^2 values of the Boyd model for AC-Z2-700 and AC-K2-700 vary between 0.2745 and 0.3589 and between 0.1890 and 0.4626, respectively. These low values indicate that the Boyd model cannot adequately represent the diffusion process for these samples. The fact that the lines drawn from the Boyd equation do not pass through the origin and the regression coefficients are low also indicates that intraparticle diffusion is not the sole mechanism controlling the adsorption process.

It is seen that the curves obtained for the Weber–Morris equation do not pass through the origin and consist of two intersecting lines with different slopes. This shows that intraparticle diffusion is not the factor that completely controls the process. This indicates that external diffusion effects or other kinetic processes (e.g., surface adsorption) also play a role and thus the adsorption has a complex dynamics. The slopes of the first curves in Figure 11 are higher. The R^2 values for the first part of AC-Z2-700 vary in the range of 0.9565–0.9746 and for the second part, 0.1449–0.3240; and the R^2 values for the first part of AC-K2-700 vary in the range of 0.6418–0.9760 and for the second part, 0.0797–0.4836. For the first part of the Weber–Morris model, the k_2 values range from 22.47 to 84.11 μmol/g min$^{0.5}$ for AC-Z2-700 and from 9.80 to 66.05 μmol/g min$^{0.5}$ for AC-K2-700, which reveals that the Weber–Morris model represents the intraparticle diffusion process more consistently, as the linearity observed in the initial stage of the plots and the relatively high k_2 values indicate that intraparticle diffusion is a significant contributor to the overall adsorption rate under the studied conditions.

As a result, the generally low R^2 values of the Boyd model support that this model cannot adequately represent intraparticle diffusion processes, while the Weber–Morris model provides good agreement with higher R^2 values in almost all cases. These findings reveal the effectiveness of the Boyd and Weber–Morris models in evaluating intraparticle diffusion processes and emphasize that the Weber–Morris model is a more reliable alternative. In general, these results are also important in terms of understanding the kinetic behaviors of various adsorbates on different sample surfaces of the relevant models. For example, it was observed that intraparticle diffusion was an important mechanism in the adsorption process of methyl violet and methylene blue on the sepiolite surface, that the adsorption occurred with a rapid start and slowed down over time, which revealed the complex structure of the mechanism and the interactions of the adsorbed molecules with each other [80]. In another study, the removal of maxilon blue 5G dye on sepiolite was investigated, and the removal mechanism was tried to be elucidated. Weber–Morris analyses showed that adsorption occurs in two stages; surface adsorption occurs in the first stage, and the intra-particle diffusion process occurs in the second stage. These findings provided important information for understanding the dynamics of the adsorption process and for optimization studies [81]. In addition, the kinetics and mechanism of adsorption of methyl violet to the perlite surface were also tried to be elucidated. Experimental results obtained according to the Weber–Morris equation showed that the adsorption was diffusion controlled [78]. In light of the above explanations, the intraparticle diffusion mechanism of hydrogen into the pores of AC is visualized in Figure 12.

3.5 | Conclusions

In this study, ACs produced from sunflower stalks by chemical activation ($ZnCl_2$ and KOH) followed by carbonization were optimized using BET, FTIR, DTA/TG, and SEM/EDX techniques, and their hydrogen storage capacities were systematically evaluated. The optimum production conditions were identified as a chemical agent/biomass ratio of 2:1 and a carbonization temperature of 700°C, yielding the highest surface area and micropore volumes for both $ZnCl_2$- and KOH-activated samples. FTIR analysis revealed the loss of lignin and cellulose characteristics and the formation of aromatic functional groups. Thermal analysis showed that while sunflower stalk and AC-K2-700 decomposed in three steps, AC-Z2-700 exhibited four-step decomposition behavior. SEM results demonstrated that $ZnCl_2$ activation promoted a more developed microporous structure compared to KOH activation. The higher micropore volume of AC-Z2-700 (compared to AC-K2-700) resulted in a superior hydrogen storage capacity.

At room temperature, hydrogen storage increased proportionally with gas pressure for both samples, consistent with Henry's law. At cryogenic temperatures, hydrogen storage capacities were significantly higher, and excess adsorption phenomena were observed, with the Langmuir isotherm providing the best fit. AC-Z2-700 achieved the highest hydrogen storage capacity under cryogenic conditions. Kinetic analysis revealed that hydrogen adsorption followed **a** pseudo-second-order model ($R^2 > 0.99$) and was mainly controlled by intraparticle diffusion, reaching equilibrium within approximately 2 min.

Overall, this study demonstrates that sunflower stalks can serve as a sustainable and low-cost precursor for producing high surface area ACs with competitive hydrogen storage capacities, particularly when activated with $ZnCl_2$. Findings from earlier research indicate that utilizing agricultural residues as sources for carbon production offers dual benefits: it transforms biomass waste into valuable materials and alleviates the environmental impacts linked to the extraction and disposal of raw materials. In contrast to the manufacture of ACs from coal, carbons obtained from agricultural wastes typically demand less energy during both pyrolysis and activation stages. Furthermore, their origin from renewable resources plays a role in lowering total CO_2 emissions. When combined with their cost advantages and competitive performance, these environmental gains emphasize the strong potential of sunflower stalk-derived ACs for eco-friendly hydrogen storage technologies.

Acknowledgments

This work was supported by Balikesir University (Project Number: BAP2018/105).

Conflicts of Interest

The authors declare no conflicts of interest.

Data Availability Statement

The data that support the findings of this study are available on request from the corresponding author. The data are not publicly available due to privacy or ethical restrictions.

References

1. S. Y. Lee and S. J. Park, “Effect of Temperature on Activated Carbon Nanotubes for Hydrogen Storage Behaviors,” *International Journal of Hydrogen Energy* 35 (2010): 6757–6762, https://doi.org/10.1016/j.ijhydene.2010.03.114.

2. E. E. Doğan, “Hydrogen Production and Its Storage From Solar Energy,” *Advances in Materials Science* 20, no. 2 (2020): 14–25, https://doi.org/10.2478/adms-2020-0007.

3. W. Zhao, V. Fierro, C. Zlotea, et al., “Optimization of Activated Carbons for Hydrogen Storage,” *International Journal of Hydrogen Energy* 36 (2011): 11746–11751, https://doi.org/10.1016/j.ijhydene.2011.05.181.

4. I. Wrobel-Iwaniec, N. Diez, and G. Gryglewicz, “Chitosan-Based Highly Activated Carbons for Hydrogen Storage,” *International Journal of Hydrogen Energy* 40 (2015): 5788–5796, https://doi.org/10.1016/j.ijhydene.2015.03.034.

5. Ü. Çakır, F. Kestel, B. Koçer Kızılduman, Z. Bicil, and M. Doğan, “Multi Walled Carbon Nanotubes Functionalized by Hydroxyl and Schiff Base and Their Hydrogen Storage Properties,” *Diamond and Related Materials* 120 (2021): 108604, https://doi.org/10.1016/j.diamond.2021.108604.

6. Ü. Çakir, M. Doğan, B. K. Kizilduman, and Z. Bicil, “Functionalized and Schiff Base Based Multi Walled Carbon Nanotubes for Hydrogen Storage,” *Journal of Alloys and Compounds* 1010 (2025): 177290, https://doi.org/10.1016/j.jallcom.2024.177290.

7. M. Sevilla and R. Mokaya, “Energy Storage Applications of Activated Carbons: Supercapacitors and Hydrogen Storage,” *Energy & Environmental Science* 7 (2014): 1250–1280, https://doi.org/10.1039/C3EE43525C.

8. T. Manda, G. O. Barasa, H. Louis, et al., “A Data-Guided Approach for the Evaluation of Zeolites for Hydrogen Storage With the Aid of Molecular Simulations,” *Journal of Molecular Modeling* 30 (2024): 43, https://doi.org/10.1007/s00894-024-05837-z.

9. H. B. Albargi, A. Abbas, M. Zeeshan, et al., “Design of Iron-Based Metal-Organic Framework (Fe-MOF) and Molybdenum Telluride ($MoTe_2$) Nanohybrids for Enhanced Energy Storage and Hydrogen Evolution Reactions,” *Inorganic Chemistry Communications* 173 (2025): 113791, https://doi.org/10.1016/j.inoche.2024.113791.

10. K. S. Nivedhitha, R. Venkatesh, N. R. Banapurmath, et al., “Graphene Enhanced Mg–Ni–Ti Nanocomposites for Hydrogen Storage Application,” *International Journal of Hydrogen Energy* 102 (2025): 972–979, https://doi.org/10.1016/j.ijhydene.2025.01.090.

11. N. F. T. Arifin, N. Yusof, N. A. H. M. Nordin, et al., “Comparison of Different Activated Agents on Biomass-Derived Graphene Towards the Hybrid Nanocomposites With Zeolitic Imidazolate Framework-8 for Room Temperature Hydrogen Storage,” *Journal of Environmental Chemical Engineering* 9, no. 2 (2021): 105118, https://doi.org/10.1016/j.jece.2021.105118.

12. M. Doğan, A. Selek, O. Turhan, B. K. Kızılduman, and Z. Bicil, “Different Functional Groups Functionalized Hexagonal Boron Nitride (h-BN) Nanoparticles and Multi-Walled Carbon Nanotubes (MWCNT) for Hydrogen Storage,” *Fuel* 303 (2021): 121335, https://doi.org/10.1016/j.fuel.2021.121335.

13. F. N. Yalçınkaya, M. Doğan, Z. Bicil, and B. K. Kizilduman, “Effect of Functionalization and Li-Doping Methods to Hydrogen Storage Capacities of MWCNTs,” *Fuel* 372 (2024): 132274, https://doi.org/10.1016/j.fuel.2024.132274.

14. Z. Bicil, “Adsorptıon Kinetics and Mechanism of Hydrogen on Pristine and Functionalized Multi-Walled Carbon Nanotubes,” *Fuel* 403 (2025): 136130, https://doi.org/10.1016/j.fuel.2025.136130.

15. M. Doğan, M. Y. Kalafat, B. K. Kızılduman, et al., “Hydrogen Storage Analysis of Fullerene and Defective Fullerenes: The First Experimental Study,” *Fuel* 390 (2025): 134705, https://doi.org/10.1016/j.fuel.2025.134705.

16. Z. Bicil and M. Doğan, “Characterization of Activated Carbons Prepared From Almond Shells and Their Hydrogen Storage Properties,”

Energy & Fuels 35 (2021): 10227–10240, https://doi.org/10.1021/acs.energyfuels.1c00795.

17. A. Turkyilmaz, M. Doğan, and M. Alkan, "Characterization and Adsorptive Properties of Activated Carbon Prepared From Olive Stones," *Fresenius Environmental Bulletin* 23, no. 7A (2014): 1585–1593.

18. A. Turkyilmaz, K. Isinkaralar, M. Dogan, B. K. Kizilduman, and Z. Bicil, "Production, Characterization, and Hydrogen Storage Properties of Activated Carbon From Horse Chestnut Shell," *Sustainable Chemistry and Pharmacy* 40 (2024): 101634, https://doi.org/10.1016/j.scp.2024.101634.

19. A. Turkyilmaz, M. Doğan, and M. Alkan, "Surface and Adsorptive Properties of Activated Carbon Prepared From Pomegranate Shell," *Fresenius Environmental Bulletin* 22, no. 11A (2013): 3317–3325.

20. S. Beak, S. Kim, S. Oh, and J. Bae, "Lignin-Based Porous Carbon for Efficient Hydrogen Storage," *Journal of Environmental Chemical Engineering* 13 (2025): 116086, https://doi.org/10.1016/j.jece.2025.116086.

21. M. Doğan, P. Sabaz, Z. Bicil, B. Koçer Kızılduman, and Y. Turhan, "Activated Carbon Synthesis From Tangerine Peel and Its Use in Hydrogen Storage," *Journal of the Energy Institute* 93 (2020): 2176–2185, https://doi.org/10.1016/j.joei.2020.05.011.

22. K. Soukup, V. Hejtmánek, G. J. F. Cruz, V. Jandová, and O. Solcova, "Excess Adsorption Isotherms of Hydrogen on Activated Carbons From Agricultural Waste Materials," *Chemical Engineering and Technology* 40 (2017): 900–906, https://doi.org/10.1002/ceat.201600610.

23. N. Ataman and L. Şık, "*Helianthus annuus* L.: Comparison of the Properties of Fibers Obtained From the Plant by Methods of Decortication and Retting," *Celal Bayar University Journal of Science* 19 (2023): 359–366, https://doi.org/10.18466/cbayarfbe.1366612.

24. S. Caparrós, J. Ariza, F. López, J. A. Nacimiento, G. Garrote, and L. Jiménez, "Hydrothermal Treatment and Ethanol Pulping of Sunflower Stalks," *Bioresource Technology* 99, no. 5 (2008): 1368–1372, https://doi.org/10.1016/j.biortech.2007.01.045.

25. X. Wang, S. Yun, W. Fang, et al., "Layer-Stacking Activated Carbon Derived From Sunflower Stalk as Electrode Materials for High-Performance Supercapacitors," *ACS Sustainable Chemistry & Engineering* 6 (2018): 1–26, https://doi.org/10.1021/acssuschemeng.8b01334.

26. M. Baysal, K. Bilge, B. Yılmaz, M. Papila, and Y. Yürüm, "Preparation of High Surface Area Activated Carbon From Waste-Biomass of Sunflower Piths: Kinetics and Equilibrium Studies on the Dye Removal," *Journal of Environmental Chemical Engineering* 6 (2018): 1702–1713, https://doi.org/10.1016/j.jece.2018.02.020.

27. K. Y. Foo and B. H. Hameed, "Preparation and Characterization of Activated Carbon From Sunflower Seed Oil Residue via Microwave Assisted K_2CO_3 Activation," *Bioresource Technology* 102 (2011): 9794–9799, https://doi.org/10.1016/j.biortech.2011.08.007.

28. E. E. Doğan, P. Tokcan, and B. K. Kizilduman, "Storage of Hydrogen in Activated Carbons and Carbon Nanotubes," *Advanced Materials Science* 18, no. 4 (2018): 58, https://doi.org/10.1515/adms-2017-0045.

29. B. K. Kızılduman, Y. Turhan, and M. Doğan, "Mesoporous Carbon Spheres Produced by Hydrothermal Carbonization From Rice Husk: Optimization, Characterization and Hydrogen Storage," *Advanced Powder Technology* 32, no. 11 (2021): 4222–4234, https://doi.org/10.1016/j.apt.2021.09.025.

30. Z. S. Doğan, E. E. Doğan, Z. Bicil, and B. K. Kizilduman, "The Effect of Li-Doping and Doping Methods to Hydrogen Storage Capacities of Some Carbonaceous Materials," *Fuel* 396 (2025): 135280, https://doi.org/10.1016/j.fuel.2025.135280.

31. M. Thommes, K. Kaneko, A. V. Neimark, et al., "Physisorption of Gases, With Special Reference to the Evaluation of Surface Area and Pore Size Distribution (IUPAC Technical Report)," *Pure and Applied Chemistry* 87, no. 9–10 (2015): 1051–1069.

32. N. E. Williams, O. A. Oba, and N. P. Aydinlik, "Modification, Production, and Methods of KOH-Activated Carbon," *ChemBioEng Reviews* 9, no. 2 (2022): 164–189, https://doi.org/10.1002/cben.202100030.

33. M. Kwiatkowski, E. Broniek, V. Fierro, and A. Celzard, "An Evaluation of the Impact of the Amount of Potassium Hydroxide on the Porous Structure Development of Activated Carbons," *Materials* 14 (2021): 2045, https://doi.org/10.3390/ma14082045.

34. A. Alfarra, E. Frackowiak, and F. Béguin, "The HSAB Concept as a Means to Interpret the Adsorption of Metal Ions Onto Activated Carbons," *Applied Surface Science* 228 (2004): 84–92, https://doi.org/10.1016/j.apsusc.2003.12.033.

35. B. Li, C. Li, D. Li, et al., "Activation of Pine Needles With Zinc Chloride: Evolution of Functionalities and Structures of Activated Carbon Versus Increasing Temperature," *Fuel Processing Technology* 252 (2023): 107987, https://doi.org/10.1016/j.fuproc.2023.107987.

36. A. Ahmadpour and D. D. Do, "The Preparation of Activated Carbon From Macadamia Nutshell by Chemical Activation," *Carbon* 35, no. 12 (1997): 1723–1732, https://doi.org/10.1016/S0008-6223(97)00127-9.

37. K. Mohanty, M. Jha, B. C. Meikap, and M. N. Biswas, "Removal of Chromium (VI) From Dilute Aqueous Solutions by Activated Carbon Developed From *Terminalia Arjuna* Nuts Activated With Zinc Chloride," *Chemical Engineering Science* 60, no. 11 (2005): 3049–3059, https://doi.org/10.1016/j.ces.2004.12.049.

38. İ. Demiral, C. Şamdan, and H. Demiral, "Production and Characterization of Activated Carbon by Zinc Chloride Activation From Peach Stone," *Eskişehir Osmangazi University Journal of Engineering and Architecture* 28, no. 1 (2020): 73–82, https://doi.org/10.31796/ogummf.606556.

39. M. F. Dilekoglu and M. Yapici, "Adsorption of Naproxen Pharmaceutical Micropollutant From Aqueous Solutions on Superior Activated Carbon Synthesized From Sheep Manure: Kinetics, Thermodynamics, and Mechanism," *Journal of Molecular Liquids* 381 (2023): 121839, https://doi.org/10.1016/j.molliq.2023.121839.

40. E. Yagmur, Y. Gokce, S. Tekin, N. I. Semerci, and Z. Aktas, "Characteristics and Comparison of Activated Carbons Prepared From Oleaster (*Elaeagnus Angustifolia* L.) Fruit Using KOH and $ZnCl_2$," *Fuel* 267 (2020): 117232, https://doi.org/10.1016/j.fuel.2020.117232.

41. F. Ateş and Ö. Özcan, "Preparation and Characterization of Activated Carbon From Poplar Sawdust by Chemical Activation: Comparison of Different Activating Agents and Carbonization Temperature," *European Journal of Engineering and Technology Research* 3, no. 11 (2018): 6–11, https://doi.org/10.24018/ejeng.2018.3.11.939.

42. S. Suhdi and S.-C. Wang, "Fine Activated Carbon From Rubber Fruit Shell Prepared by Using $ZnCl_2$ and KOH Activation," *Applied Sciences* 11 (2021): 3994, https://doi.org/10.3390/app11093994.

43. X. F. He, L. Yang, H. J. Wu, N. Liu, Y. G. Zhang, and A. N. Zhou, "Characterization and Pyrolysis Behaviors of Sunflower Stalk and Its Hydrolysis Residue," *Asia-Pacific Journal of Chemical Engineering* 11, no. 5 (2016): 803–811, https://doi.org/10.1002/apj.2015.

44. Y. Guo and Q. Wang, "Fabrication and Characterization of Activated Carbon From *Phyllostachys Edulis* Using Single-Step KOH Activation With Different Temperatures," *PRO* 10, no. 9 (2022): 1712, https://doi.org/10.3390/pr10091712.

45. A. Zabaniotou, O. Ioannidou, E. Antonakou, and A. Lappas, "Experimental Study of Pyrolysis for Potential Energy, Hydrogen and Carbon Material Production From Lignocellulosic Biomass," *International Journal of Hydrogen Energy* 33, no. 10 (2008): 2433–2444, https://doi.org/10.1016/j.ijhydene.2008.02.080.

46. M. X. Fang, D. K. Shen, Y. X. Li, C. J. Yu, Z. Y. Luo, and K. F. Cen, “Kinetic Study on Pyrolysis and Combustion of Wood Under Different Oxygen Concentrations by Using TG-FTIR Analysis,” *Journal of Analytical and Applied Pyrolysis* 77 (2006): 22–27, https://doi.org/10.1016/j.jaap.2005.12.010.

47. K. Isinkaralar, G. Gullu, A. Turkyilmaz, M. Dogan, and O. Turhan, “Activated Carbon Production From Horse Chestnut Shells for Hydrogen Storage,” *International Journal of Global Warming* 26, no. 4 (2022): 361–373, https://doi.org/10.1504/IJGW.2022.122430.

48. G. Zhu, X. Deng, M. Hou, et al., “Comparative Study on Characterization and Adsorption Properties of Activated Carbons by Phosphoric Acid Activation From Corn Cob and Its Acid and Alkaline Hydrolysis Residues,” *Fuel Processing Technology* 144 (2016): 255–261, https://doi.org/10.1016/j.fuproc.2016.01.007.

49. A. H. Basta, V. Fierro, H. El-Saied, and A. Celzard, “2-Steps KOH Activation of Rice Straw: An Efficient Method for Preparing High-Performance Activated Carbons,” *Bioresource Technology* 100 (2009): 3941–3947, https://doi.org/10.1016/j.biortech.2009.02.028.

50. F. Caturla, M. Molina-Sabio, and F. Rodríguez-Reinoso, “Preparation of Activated Carbon by Chemical Activation With ZnCl2,” *Carbon* 29 (1991): 999–1007, https://doi.org/10.1016/0008-6223(91)90179-M.

51. T. Uysal, G. Duman, Y. Önal, I. Yasa, and J. Yanik, “Production of Activated Carbon and Fungicidal Oil From Peach Stone by Two-Stage Process,” *Journal of Analytical and Applied Pyrolysis* 108 (2014): 47–55, https://doi.org/10.1016/j.jaap.2014.05.017.

52. F. Mbarki, T. Selmi, A. Kesraoui, and M. Seffen, “Low-Cost Activated Carbon Preparation From Corn Stigmata Fibers Chemically Activated Using H_3PO_4, $ZnCl_2$ and KOH: Study of Methylene Blue Adsorption, Stochastic Isotherm and Fractal Kinetic,” *Industrial Crops and Products* 178 (2022): 114546, https://doi.org/10.1016/j.indcrop.2022.114546.

53. H. S. Karapınar, “Adsorption Performance of Activated Carbon Synthesis by $ZnCl_2$, KOH, H_3PO_4 With Different Activation Temperatures From Mixed Fruit Seeds,” *Environmental Technology* 43, no. 9 (2022): 1417–1435, https://doi.org/10.1080/09593330.2021.1968507.

54. R. Nedjai, N. A. Kabbashi, M. Z. Alam, and M. F. R. Al-Khatib, “Production and Characterization of Activated Carbon From Baobab Fruit Shells by Chemical Activation Using $ZnCl_2$, H_3PO_4 and KOH,” *Journal of Physics: Conference Series* 2129, no. 1 (2021): 012009, https://doi.org/10.1088/1742-6596/2129/1/012009.

55. H. Marsh and F. R. Reinoso, *Activated Carbon* (Elsevier, 2006).

56. S. Surkan, C. M. Mendez, and M. G. Maiocchi, “Characterization of Activated Carbon Produced From Industrial Waste of Yerba Mate by Chemical Activation With $ZnCl_2$,” *Revista de Ciencia y Tecnología* 42, no. 1 (2024): 65–71.

57. W. Spencer, D. Ibana, P. Singh, and A. N. Nikoloski, “Effect of Surface Area, Particle Size and Acid Washing on the Quality of Activated Carbon Derived From Lower Rank Coal by KOH Activation,” *Sustainability* 16, no. 14 (2024): 5876, https://doi.org/10.3390/su16145876.

58. A. D. Ardianti, “Activation of $ZnCl_2$ and KOH Carbon From Bark of *Salak Wedi* as a Material for Making Supercapacitor Electrodes,” *Science Education and Application Journal* 4, no. 1 (2022): 37–45.

59. N. Samghouli, I. Bencheikh, K. Azoulay, S. Jansson, and S. El Hajjaji, “Mechanistic and Reactional Activation Study of Carbons Destined for Emerging Pharmaceutical Pollutant Adsorption,” *Environmental Monitoring and Assessment* 197, no. 3 (2025): 259, https://doi.org/10.1007/s10661-025-13685-4.

60. A. C. Lua and T. Yang, “Characteristics of Activated Carbon Prepared From Pistachio-Nut Shell by Zinc Chloride Activation Under Nitrogen and Vacuum Conditions,” *Journal of Colloid and Interface Science* 290, no. 2 (2005): 505–513, https://doi.org/10.1016/j.jcis.2005.04.063.

61. N. P. Stadie, J. J. Vajo, R. W. Cumberland, A. A. Wilson, C. C. Ahn, and B. Fultz, “Zeolite-Templated Carbon Materials for High-Pressure Hydrogen Storage,” *Langmuir* 28, no. 26 (2012): 10057–10063, https://doi.org/10.1021/la302050m.

62. J. M. Sousa, A. L. Ferreira, D. P. Fagg, E. Titus, R. Krishna, and J. Gracio, “Temperature Dependence of the Henry's Law Constant for Hydrogen Storage in NaA Zeolites: A Monte Carlo Simulation Study,” *Journal of Nanoscience and Nanotechnology* 12 (2012): 6785–6791, https://doi.org/10.1166/jnn.2012.4569.

63. Y. J. Heo and S. J. Park, “Synthesis of Activated Carbon Derived From Rice Husks for Improving Hydrogen Storage Capacity,” *Journal of Industrial and Engineering Chemistry* 31 (2015): 330–334, https://doi.org/10.1016/j.jiec.2015.07.006.

64. E. Poirier, R. Chahine, and T. K. Bose, “Hydrogen Adsorption in Carbon Nanostructures,” *International Journal of Hydrogen Energy* 26, no. 8 (2001): 831–835, https://doi.org/10.1016/S0360-3199(01)00014-3.

65. R. Ströbel, J. Garche, P. T. Moseley, L. Jörissen, and G. Wolf, “Hydrogen Storage by Carbon Materials,” *Journal of Power Sources* 159, no. 2 (2006): 781–801, https://doi.org/10.1016/j.jpowsour.2006.03.047.

66. N. M. Musyoka, M. Wdowin, K. M. Rambau, et al., “Synthesis of Activated Carbon From High-Carbon Coal Fly Ash and Its Hydrogen Storage Application,” *Renewable Energy* 155 (2020): 1264–1271, https://doi.org/10.1016/j.renene.2020.04.003.

67. N. Bader, R. Zacharia, O. Abdelmottale, and D. Cossement, “How the Activation Process Modifies the Hydrogen Storage Behavior of Biomass-Derived Activated Carbons,” *Journal of Porous Materials* 25 (2018): 221–234, https://doi.org/10.1007/s10934-017-0436-8.

68. T. Ramesh, N. Rajalakshmi, and K. S. Dhathathreyan, “Activated Carbons Derived From Tamarind Seeds for Hydrogen Storage,” *Journal of Energy Storage* 4 (2015): 89–95, https://doi.org/10.1016/j.est.2015.09.005.

69. M. Vadi, A. O. Mansoorabad, M. Mohammadi, and N. Rostami, “Investigation of Langmuir, Freundlich and Temkin Adsorption Isotherm of Tramadol by Multi-Wall Carbon Nanotube,” *Asian Journal of Chemistry* 25 (2013): 5467–5469, https://doi.org/10.14233/ajchem.2013.14786.

70. P. Benard and R. Chahine, “Determination of the Adsorption Isotherms of Hydrogen on Activated Carbons Above the Critical Temperature of the Adsorbate Over Wide Temperature and Pressure Ranges,” *Langmuir* 17 (2001): 1950–1955, https://doi.org/10.1021/la001381x.

71. A. Al-Hajjaj, B. Zamora, A. A. Shah, E. Reguera, D. V. Bavykin, and F. C. Walsh, “On the Application of Standard Isotherms to Hydrogen Adsorption in Microporous Materials,” *International Journal of Hydrogen Energy* 36 (2011): 14464–14476, https://doi.org/10.1016/j.ijhydene.2011.07.110.

72. M. Eriksson, I. Lundström, and L. G. Ekedahl, “A Model of the Temkin Isotherm Behavior for Hydrogen Adsorption at Pd–SiO_2 Interfaces,” *Journal of Applied Physics* 82 (1997): 3143–3146, https://doi.org/10.1063/1.366158.

73. X. Z. Chu, Y. P. Zhou, Y. Z. Zhang, W. Su, Y. Sun, and L. Zhou, “Adsorption of Hydrogen Isotopes on Micro- and Mesoporous Adsorbents With Orderly Structure,” *Journal of Physical Chemistry. B* 110 (2006): 22596–22600, https://doi.org/10.1021/jp064745o.

74. M. K. Kazankapova, B. T. Yermagambet, U. M. Kozhamuratova, et al., “Obtaining and Investigating Sorption Capacity of Carbon Nanomaterials Derived From Coal for Hydrogen Storage,” *ES Energy & Environment* 25 (2024): 1234, https://doi.org/10.30919/esee1234.

75. A. A. Haidry, Y. Jia, A. Raza, H. Zhu, A. Zavabeti, and B. Saruhan, “Elucidating the Hydrogen Adsorption Kinetics on Pt/TiO_2/Pt Based Highly Efficient Sensors,” *Materials Research Bulletin* 167 (2023): 112415, https://doi.org/10.1016/j.materresbull.2023.112415.

76. I. Matsumoto, K. Asano, K. Sakaki, and Y. Nakamura, "Hydrogen Absorption Kinetics of Magnesium Fiber Prepared by Vapor Deposition," *International Journal of Hydrogen Energy* 36, no. 22 (2011): 14488–14495, https://doi.org/10.1016/j.ijhydene.2011.08.029.

77. S. V. Sawant, M. D. Yadav, S. Banerjee, A. W. Patwardhan, J. B. Joshi, and K. Dasgupta, "Hydrogen Storage in Boron-Doped Carbon Nanotubes: Effect of Dopant Concentration," *International Journal of Hydrogen Energy* 46 (2021): 39297–39314, https://doi.org/10.1016/j.ijhydene.2021.09.183.

78. M. Doğan and M. Alkan, "Adsorption Kinetics of Methyl Violet Onto Perlite," *Chemosphere* 50 (2003): 517–528, https://doi.org/10.1016/S0045-6535(02)00629-X.

79. G. E. Boyd, A. W. Adamson, and L. S. Myers, "The Exchange Adsorption of Ions From Aqueous Solutions by Organic Zeolites. II. Kinetics," *Journal of the American Chemical Society* 69 (1947): 2836–2848, https://doi.org/10.1021/ja01203a066.

80. M. Doğan, Y. Özdemir, and M. Alkan, "Adsorption Kinetics and Mechanism of Cationic Methyl Violet and Methylene Blue Dyes Onto Sepiolite," *Dyes and Pigments* 75 (2007): 701–713, https://doi.org/10.1016/j.dyepig.2006.07.023.

81. M. Alkan, M. Doğan, Y. Turhan, Ö. Demirbaş, and P. Turan, "Adsorption Kinetics and Mechanism of Maxilon Blue 5G Dye on Sepiolite From Aqueous Solutions," *Chemical Engineering Journal* 139 (2008): 213–223, https://doi.org/10.1016/j.cej.2007.07.080.